Fabrication of close-packed non-circular nanomagnetic pattern using low energy self-limiting ion-milling process

A Dissertation

Presented to

the Faculty of the Department of Electrical and Computer Engineering

University of Houston

In Partial Fulfillment

of the Requirements for the Degree

Doctor of Philosophy

in Electrical Engineering

by

Zhen Zheng

May 2013

Fabrication of close-packed non-circular nanomagnetic pattern using low energy self-limiting ion-milling process

Zhen Zheng

Approved:

Chair of the Committee
Dmitri Litvinov, Professor
Electrical and Computer Engineering

Committee Members:

Paul Ruchhoeft, Associate Professor
Electrical and Computer Engineering

Jiming Bao, Assistant Professor
Electrical and Computer Engineering

Gila E. Stein, Assistant Professor
Chemical and Biomolecular Engineering

Abdelhak Bensaoula, Research Professor
Physics

Suresh K. Khator, Associate Dean
Cullen College of Engineering

Badri Roysam, Professor and Chair
Electrical and Computer Engineering

Acknowledgements

First I would like to thank my family, especially my parents, who always encouraged me in my study and life. Without their moral support, I would not be able to accomplish my achievements today.

I would like to express my sincere gratitude to my advisor, Dr. Dmitri Litvinov, for his guidance and support both in my courses and research work. I would also like to extend my gratitude to Dr. Paul Ruchhoeft for his guidance and insightful advice throughout my work here and also for serving on my committee. I am grateful to Dr Jiming Bao, Dr Gila Stein and Dr. Abdelhak Bensaoula for serving as my committee members.

I acknowledge my colleagues in my research group: Long Chang, who has always been extremely supportive, and has been there for insightful discussions, advice and help; Ivan Nekrashevich, who helped me with statistic analysis and always has brilliant ideas on research work; Wenlan Qiu and Dahye Lee, who helped me with surface analysis. Without them it would not have been possible to complete this work successfully. I would also like to take this opportunity to thank all my friends and colleagues who have supported me all the way during my time here.

Fabrication of close-packed non-circular nanomagnetic pattern using low energy self-limiting ion-milling process

An Abstract

of a

Dissertation

Presented to

the Faculty of the Department of Electrical and Computer Engineering

University of Houston

In Partial Fulfillment

of the Requirements for the Degree

Doctor of Philosophy

in Electrical Engineering

by

Zhen Zheng

May 2013

Abstract

We describe a low energy glow discharge process using a reactive-ion etching system that enables non-circular device patterns, such as squares or hexagons, to be formed from the precursor arrays of uniform circular openings in polymethyl methacrylate (PMMA), defined by electron beam lithography. This new technique is of a particular interest for bit-patterned magnetic recording medium fabrication, where square magnetic bits result in improved recording system performance. The process of generating close packed square patterns by self-limiting ion-milling (SLIM) are investigated. Results are statistically analyzed to establish optimization.

Fabrication of non-circular nanostructures has been demonstrated. Dense magnetic arrays formed by electrochemical deposition, evaporation and sputtering deposition over SLIM-formed moulds are accomplished. Applications in master production technologies such as ion beam proximity lithography and nanoimprint template manufacturing are evaluated.

New technology of magnetic patterning using low energy ion irradiation is under investigation. Helium ions strike a cobalt oxide layer to remove oxygen from a non-magnetic oxidized material, resulting in the recovery of magnetic properties of cobalt in an exposed area. The thin film of the cobalt layer turning from cobalt oxide by 120eV helium irradiation has been demonstrated. Pattern fabrication and investigation on multilayer irradiation are future work.

Table of Contents

List of Figures

List of Tables

Chapter 1: Introduction

1.1 Magnetic Recording

Magnetic Recording uses patterns of different magnetization to store information on a magnetic medium. This technology for a long time has played an important role in the data storage industry. From the first magnetic hard disk drive (HDD) produced by IBM in 1956, to the currently used commercial product sized in 1 inch, the magnetic recording industry has grown into a $200-billion multinational enterprise with ever growing demand for larger storage capacities.

Early time recording technology in magnetic hard disk drives was longitudinal magnetic recording. This technology stores information with the magnetization of the magnetic bits in the plane of the magnetic medium, as shown in Figure 1-1 on the following page. To increase the areal density and the overall storage capacity, the bit size needs to be reduced accordingly. At the same time, the signal to noise ratio (SNR) [1] of a recording system depends on the number of grains per bit (N) as

$$\mathrm{SNR} \sim \log(N), \tag{1-1}$$

where the number of grains per bit is preserved to maintain a SNR value allowing easy data reading process. As a result, the grain size is reduced with bit size reduction. This leads to thermal instabilities in magnetic recording media, which will be discussed below. Thermal stability limit for longitudinal recording is estimated to be reached at areal density in the range of 200 gigabits per square inch.

At the beginning of the 21st century, perpendicular recording was utilized as the new generation of recording technology in the HDD industry. In a perpendicular

recording disk, magnetization of the bits is normal to the plane of the disk whereas in longitudinal media magnetization, it is parallel to the surface of the disk, as shown in Figure 1-1. This change greatly increases the numbers of bits packed in the same area compared to longitudinal recording, which results in a significantly higher areal density and storage capacity. Also, in longitudinal magnetic recording, the adjacent 1's and 0's magnetostatically repel each other resulting in reduced data stability, while in the case of perpendicular recording, the adjacent 1'sand 0's mutually stabilize each other leading to higher thermal stability.

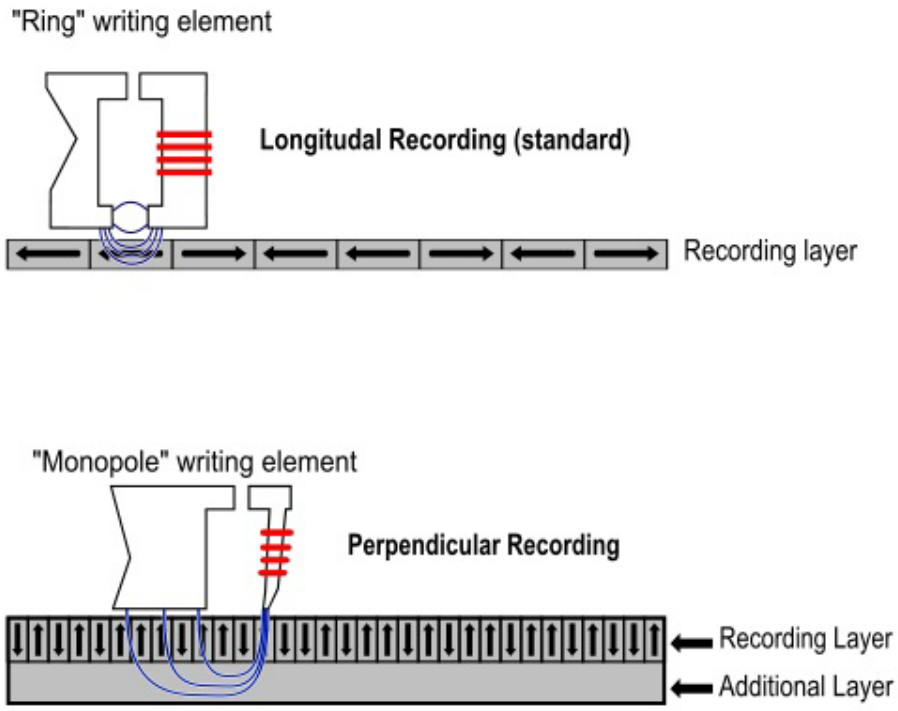

Figure 1-1: Schematic of longitudinal and perpendicular recording systems [2].

Another advantage of perpendicular recording is the utilization of a soft magnetic layer [3], which is highly permeable, buried beneath the recording layer. This soft underlayer (SUL) acts as a magnetic mirror, to effectively double the write field and the recording layer thickness. Figure 1-2 illustrates magnetic imaging by a SUL. Due to

larger write fields, higher anisotropy (Ku) and, thus, more thermally stable materials can be used as recording medium in perpendicular recording systems, leading to further increases in the areal densities as described later. Above mentioned advantages of perpendicular recording are likely to enable magnetic recording systems with areal bit densities of up to one Terabit per square inch. However, similar to longitudinal recording, perpendicular recording systems begin to suffer from thermal instabilities at 1 Tbit/in^2 areal bit density and above. New technical solutions are needed to advance magnetic storage technologies beyond the 1 Tbit/in^2 mark.

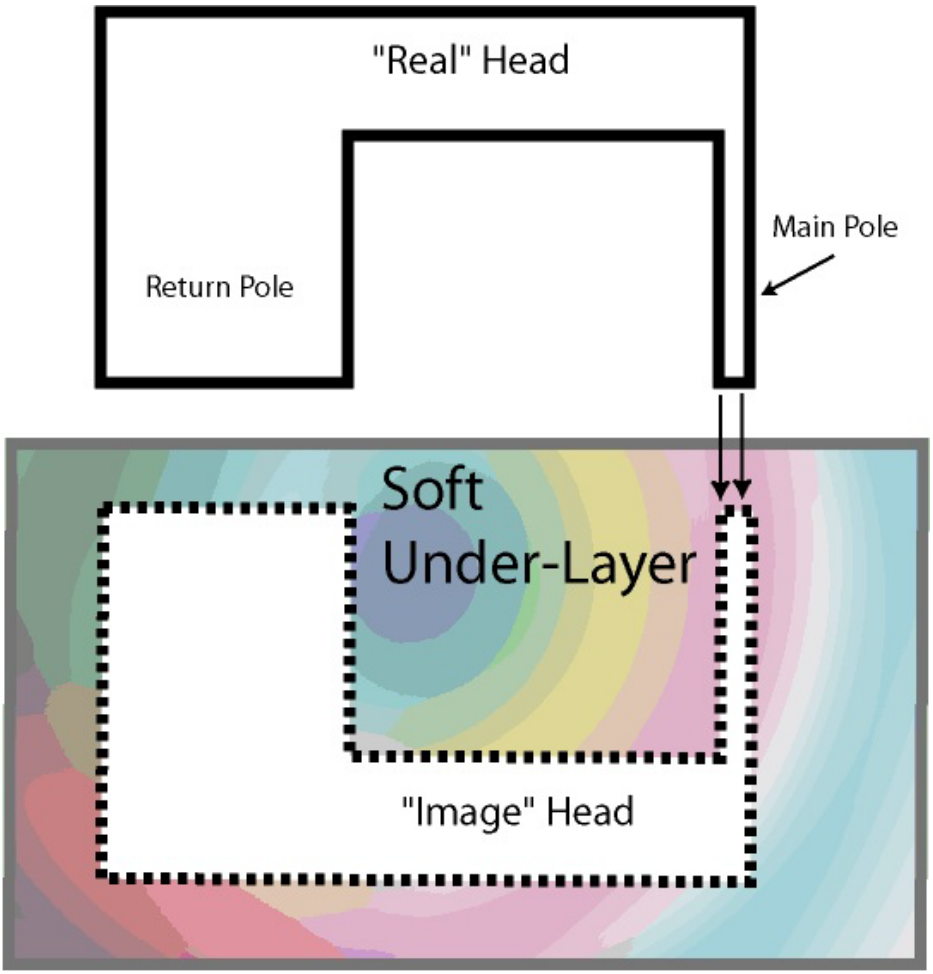

Figure 1-2: Soft underlayer (SUL) works as a magnetic mirror [4].

1.2 Superparamagnetism

When ferromagnetic or ferromagnetic materials are heated to temperature above their Curie temperature, they experience change in magnetic state to paramagnetic state. In paramagnetic state materials show weak response to applied external magnetic field and do not demonstrate coercivity characteristic to ferromagnetic state. The magnetization orientation of the material will not maintain once the external field is removed. Superparamagnetism is phenomenologically similar to paramagnetism, but occurs at temperature below the Curie point [5]. Superparamagnetic materials can be strongly magnetized by external magnetic field similar to ferromagnetic materials, but will lose the gained magnetization once external field is removed after some characteristic period of time ranging from nanoseconds to years. This phenomenon is referred as thermal instability. Obviously, whether or not the magnetic material is to be regarded as superparamagnetic or ferromagnetic depends on the “observation” time. With respect to magnetic recording, if the time for thermal instability to measurably demagnetize the medium is significantly longer than the required data retention time, then the recording layer is thought as non-superparamagnetic.

In magnetic recording, thermal instability causes random flipping of the magnetization of individual magnetic grains. If the magnetization of a significant number of magnetic grains in a recording layer is flipped, the data will be lost. The mean time between two events of spontaneous magnetization reversal of a magnetic grain is given by

$$t = \frac{1}{f_0}\exp\left(\frac{K_u V}{k_B T}\right), \tag{1-2}$$

where f_0 is the attempt frequency, an empirical constant, K_u is the magnetic anisotropy of the grain, V is its volume, k_B is the Boltzmann constant and T is the temperature. Theoretical and experimental analyses suggest that

$$\frac{K_u V}{k_B T} = 60 \sim 80, \tag{1-3}$$

ensures 10 years of reliable stable data storage, which is a widely acceptable parameter for magnetic recording [6]. Equation 1-3 points out the possible routes for future magnetic data storage developments. Since k_B is a constant and controlling temperature is not a viable industrial solution, most of the research works to develop future magnetic recording technologies are focused on increasing K_u and V.

1.3 Future Magnetic Recording

As the upper limit of perpendicular recording will be reached in several years, alternative approaches to magnetic recording have been proposed. Two of the most promising technologies are discussed below.

1.3.1 Heat Assisted Magnetic Recording

The main idea of Heat-Assisted Magnetic Recording (HAMR) is to use an extremely high magnetic anisotropy material such as FePt to keep the recording medium thermally stable when the grain size is reduced. But the coercivity of such material is so high that it is impossible to flip grain magnetization by a field generated by conventional writing head. This problem is solved by applying a laser beam along the recording head, the laser beam heats the writing bit area and increases the temperature of that area close to its Curie temperature, where the anisotropy energy reduced significantly. This approach enables writing magnetic bits into high anisotropy media [7]. Figure 1-3 shows

the schematic of HAMR. The key challenge of HAMR technology is to deliver sufficient amount of heat to localized spot which the writing head is magnetizing. One of the drawbacks of this approach is influence of neighboring bits into each other due to heat dissipation during writing process. Research on HAMR has been continued for many years now and is now under its way to come to the real product. It is believed that HAMR could enable areal densities as high as 50 Terabits per square inch.

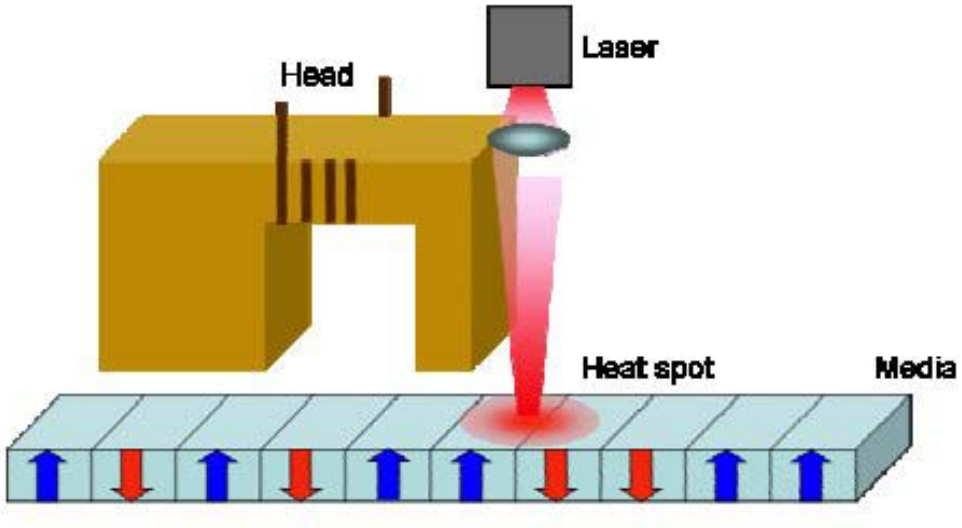

Figure 1-3: Schematic of heat assistant magnetic recording [8].

1.3.2 Bit-Patterned Medium

Bit-Patterned Medium (BPM) is another widely investigated approach for future magnetic recording application. In BPM, information is stored in bits predefined by lithography, which eliminates the randomness inherent to conventional polycrystalline magnetic recording media. Although based on polycrystalline materials, BPM is engineered to magnetize the intergranular coupling, which makes the collection of grains within a patterned bit act as one single magnetic domain, which enables higher thermal stability. Figure 1-4 shows the differences between conventional and BPM recording.

The advantages of BPM are the elimination of bit-transition [9, 10] DC noise and significant increase of the thermal activation volume. Although one Terabits per square inch demonstrations have been announced by world's leading research groups, BPM is still facing key challenges such as fabrication of dense small enough patterns with a low size distribution to keep the low reverse field distribution of the recording medium.

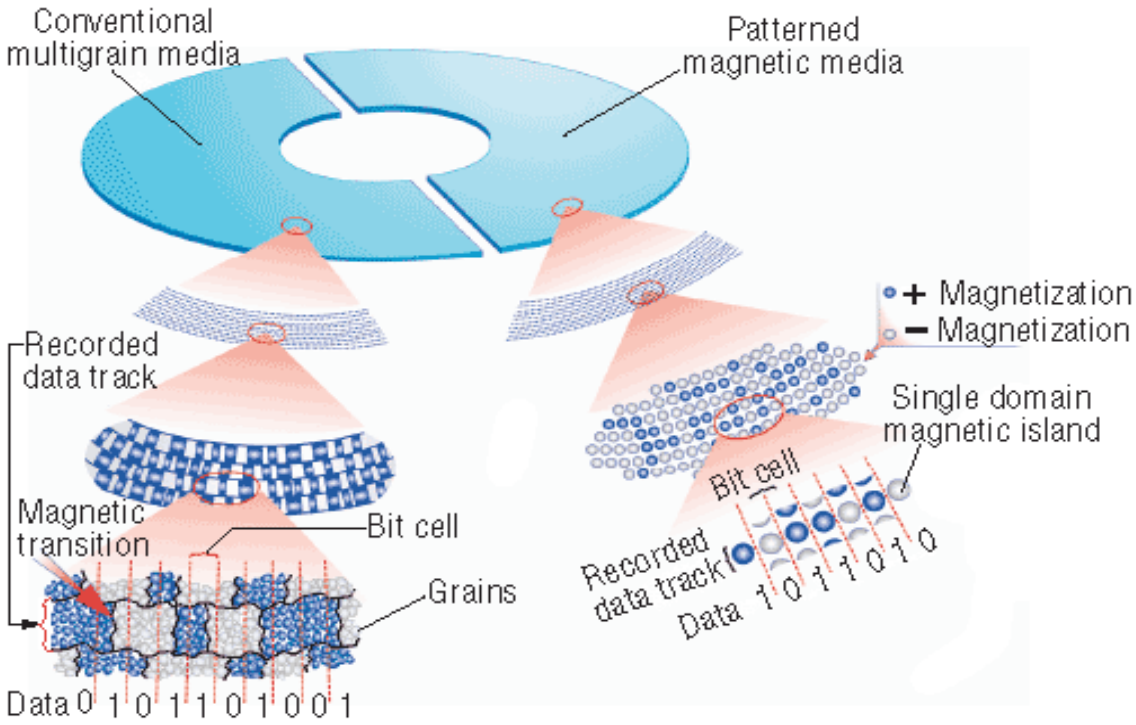

Figure 1-4: Comparison between conventional (left) and bit-patterned medium (right).

1.3.3 Shingled Magnetic Recording

The idea of Shingled Magnetic Recording (SMR) [11] was introduced later than HAMR and BPM. But SMR is much closer to the market since it uses the same mechanism as the traditional HDD and can be manufactured by current manufacturing processes with minimal change. In SMR, data is overlapping written to contiguous tracks. Therefore the tracks are squeezed for more data and the recording density is

increased. Basically, SMR is using the similar design as traditional HDDs, but with a different software and behavior. Although there are still problems need to be solved, SMR is not far from coming to the market.

1.4 Motivation

As mentioned above, BPM is one of the most promising technologies to effectively address the thermal instability challenge for future magnetic recording industry. Before it reaches its superparamagnetic limit, BPM can sustain the growth of a multibillion dollar hard disk drive industry for another 15-20 years.

My group at the University of Houston has recently developed a new fabrication approach called self-limiting ion-milling (SLIM), which enables close-packed non-circular patterns fabrication over large area at low cost. This technology is especially suitable for the application for BPM, and since the pattern it produces is non-circular, it has advantages compared to the conventional dot pattern most often utilized in BPM. These non-circular patterns provide better use of recording media. It was shown that pattern with higher density will lead to increase of magnetic coupling effect [12]. The larger pattern area, which means the larger volume, provides higher thermal stability. SLIM technology also has its potential in application in other areas which require small size non-circular patterns over a large area. My research project described here mainly focuses on the investigation of the SLIM process and the fabrication of close-packed non-circular nano patterns.

Chapter 2: Self-Limiting Ion-Milling

2.1 Lithography Background

Lithography is a process where an image is rendered in a photosensitive layer and a simple chemical development step creates the image. It has advanced significantly through the development of the modern fabrication industry. In this work, the SLIM process takes advantage of nano-size dot arrays produced by Electron Beam Lithography (EBL) and converts them into non circular patterns, like squares. This overcomes problems in EBL that are caused by the proximity effect and allows the printing process to proceed at much higher throughput.

2.1.1 Electron Beam Lithography

Electron beam lithography is the practice of scanning a focused beam of electrons over a patterned area across a surface covered with a thin layer of special sensitive polymer called resist, thereby "exposing" the resist, and of selectively removing either exposed or non-exposed regions of the resist during the development step. The purpose of this process is to create very small structures in the resist that can subsequently be transferred into the layer beneath for further purposes. With the progress of technology and requirement of smaller structure of circuits design and packing, EBL is playing a more important role in modern integrated circuit manufacturing.

2.1.2 Proximity Effect

In EBL, the resist is exposed by either scission events that break the polymer into smaller, more soluble segments (for positive resists) or by cross linking events that harden the resist by increasing the local bond density (for negative resists). These events

take place either when electrons strike the resist surface and move through the bulk or when they backscatter after multiple scattering events in the substrate. As shown in Figure 2-1, the forward scattering process is due to electron-electron interactions which deflect the primary electrons by a typically small angle, thus broadening the beam in the resist. Almost all of the electrons are not absorbed in the resist but penetrate into the substrate. These electrons can still contribute to resist exposure by scattering back into the resist at points far from the original impact location and causing subsequent inelastic/exposing processes. This backscattering process is the results of collisions with a heavy particle (i.e., substrate nucleus) and results in wide-angle scattering of the light electron from a range of depths (micrometers) in the substrate. The Rutherford backscattering probability increases quickly with substrate nuclear charge. The proximity effect [13] in EBL is the phenomenon that the exposure dose distribution, and hence the developed pattern, is wider than the scanned pattern, due to the interactions of the primary beam electrons with the resist and substrate. This causes the resist outside the scanned pattern to receive a background exposure. Although different methods [14, 15] have been developed to reduce the influence of proximity effect, none of these actually eliminates the problem.

The background exposure inherently reduces the contrast of the exposure. When printing dense features, it results in high resist etching rates even in the areas that are not exposed. As the pitch is reduced, it becomes significantly more difficult to resolve fine features. It is for this reason that most high-resolution lithography is limited to isolated features, where the proximity effect is minimal. The extra exposure also make high corner resolution pattern difficult to fabricate. Since sharp corner requires high resolution

and accurate amount of exposure to produce, the influence from extra exposure becomes more serious. When desired pattern size goes down to a certain level, for example below 200nm, all the sharp corners in the pattern tend to be rounded. That is why printing tiny non-circular structures using EBL usually results in dot patterns.

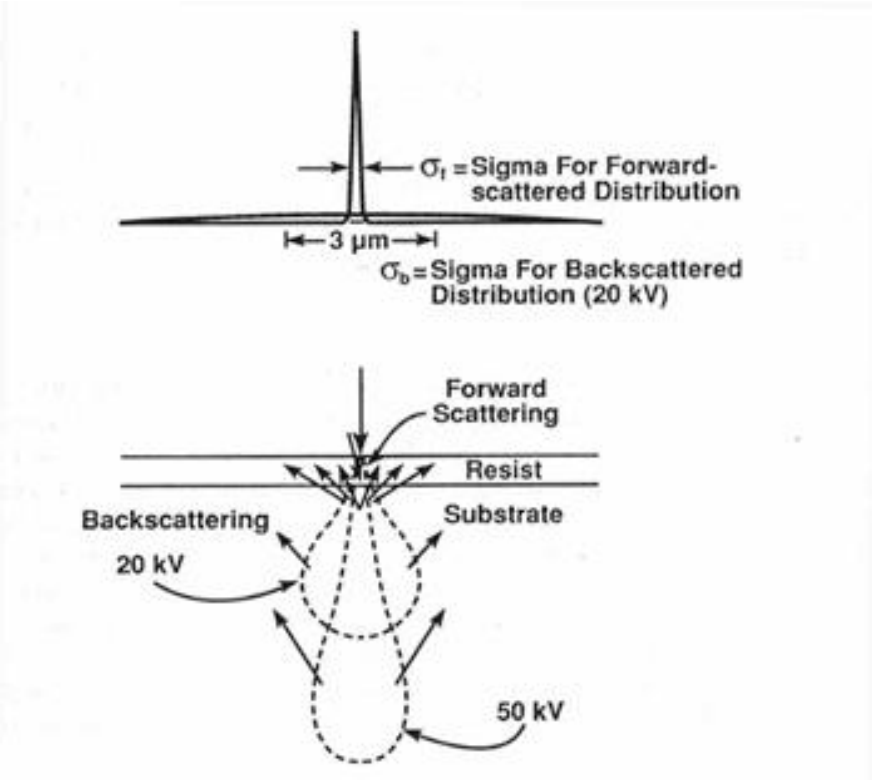

Figure 2-1: Electron scattering in electron resist exposure [17].

2.1.3 Throughput

In addition to the complexities posed by proximity effect, resolution in electron beam lithography is inversely proportional to throughput. If one wants to reduce the size of the electron beam, one needs to reduce the numerical aperture of the electron column. This is because the beam size is typically limited by spherical and chromatic aberrations whose magnitude is proportional to the numerical aperture. The result is that reducing the electron beam spot size, which is needed to define the high resolution corners of square

features, by a factor of two generally results in a fourfold reduction of the electron current. For this reason, it is extremely beneficial to first define an array of circular patterns, which can be done at much higher throughput than the squares, and then to subsequently alter the shape of the pattern. And consider the size ratio of square to circle, even if there is no influence from resolution change or aperture reduction, for each pattern, printing a square needs 27% plus more time than producing a circle. While using SLIM technique apparently requires less time and it processes the whole wafer all together.

2.2 Self-Limiting Ion-Milling Theory

SLIM is a new fabrication method developed at the Center for Integrated Bio and Nano Systems, at the University of Houston [16]. It is a simple and effective way which is especially suitable for master production of close-packed non-circular openings. Instead of improving the EBL process, SLIM uses the self-limiting property of PMMA, a common positive tone photo resist in fabrication, to change a pattern of circles into squares. This advantage lies in the fact that circles are easy and fast to print when compared to squares and one can have a profound impact on the throughput of forming such structures.

In a SLIM process, the argon ions bombard the surface of polymer film consisting of resist like PMMA, depleting oxygen and hydrogen while damaging the surface layer, turning it into a carbon-rich thin film covering the remaining resist [17]. As a result, in a lateral etching, when the wall thickness between nearby dot pattern reaches a critical value, which is about two times the carbon-rich layer thickness (~20nm), the lateral etch rate will decrease dramatically while etch rates in other directions stay the same. In this

case, the patterns would be self limited to form different non-circular shapes depending on their original grid.

Figure 2-2 is a sketch explains how SLIM works to make a square pattern. Original dot pattern is formed on a square grid using electron beam lithography. Wall thicknesses between nearby dots are different in different directions, for example, $a_0 < b_0$, as shown in the graph. The sample is then etched by argon plasma. Dot patterns expand due to lateral etching, which means the distances in every direction are decreasing. As the etching proceeds, wall thickness along a_0 reaches a critical value (a_0 is the smallest wall thickness which makes it reach first). As shown in the graph, the wall made of carbon-rich layer demonstrates significant reduction of etch rate along a_0, to a point which can even be neglected comparing to the original rate of normal (not carbon-rich) PMMA. In the meanwhile, along b_0, lateral etch rate is still the same. This phenomenon produces anisotropy in etch rate along different. In continuation of etch process, wall thicknesses along more directions reaches the critical value. Lateral etch rate change consequently, which makes the shape of original pattern change, not a dot anymore. As a result, when wall thicknesses in all directions reach the same value, which we call w, patterns change into the shape we want, such as the squares shown in the sketch.

According to our observation, the final wall thickness is about 20nm, which is twice the thickness of the carbon-rich layer. And in this sketch, the wall thickness along a_0 firstly reaches a_1, the same level as w, so it doesn't change much since then. While the thickness along b_0, is always decreasing before it reaches the final point. As we can see from Figure 2-2, square pattern has more than 27% plus area than circle pattern with the same diameter. This is especially valuable for BPM where more area leads to higher

thermal stability and recording efficiency. Even neglecting backscattering effects and assuming perfect collimation of the e-beam, it will take 20% plus more time to print each shape, while SLIM process generates square pattern on the whole wafer in a single process.

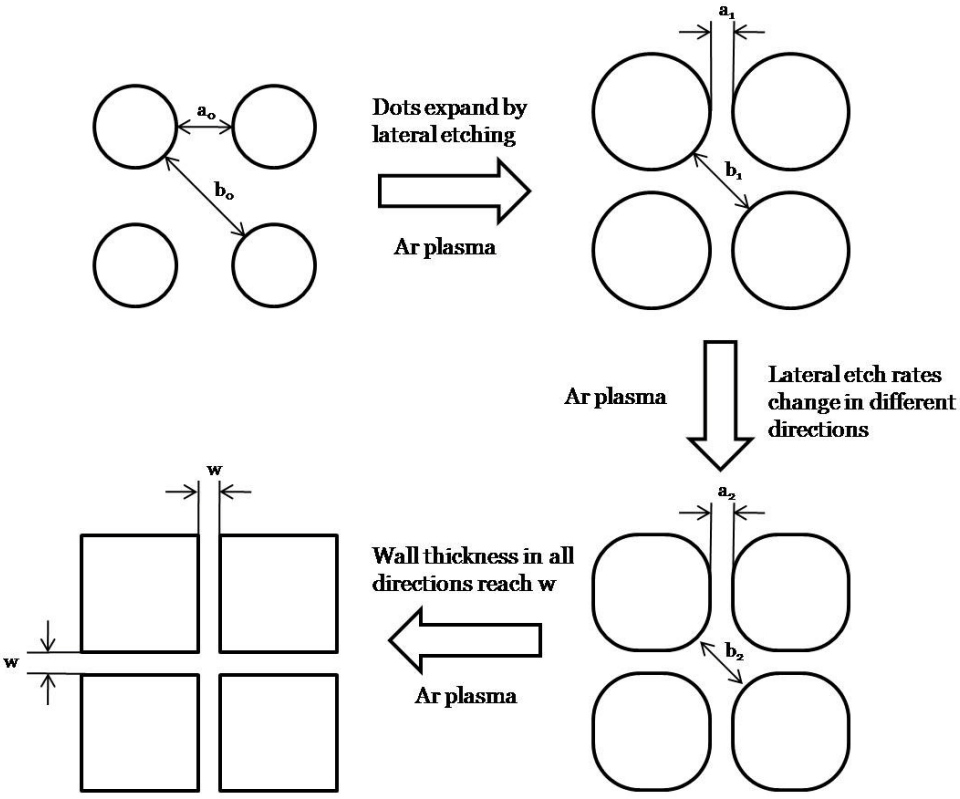

Figure 2-2: Sketch of how dot pattern turn into square pattern in SLIM process.

As we discussed above, electron beam lithography cannot print close-packed non-circular nanostructure under 200nm because of proximity effect. Besides that, even using an advanced electron beam writer will take a long time to define a single corner, since tiny beam spot is required in the corner area. SLIM, however, is the better suited technique for the solution. Figure 2-3 shows a fabricated 75nm square pattern on a 170nm PMMA layer, formed by a 2 minutes' argon etching process, from a precursor of

dot array with 60nm diameter and 90nm pitch. The square pattern can be sized down further by future optimization on the processing conditions.

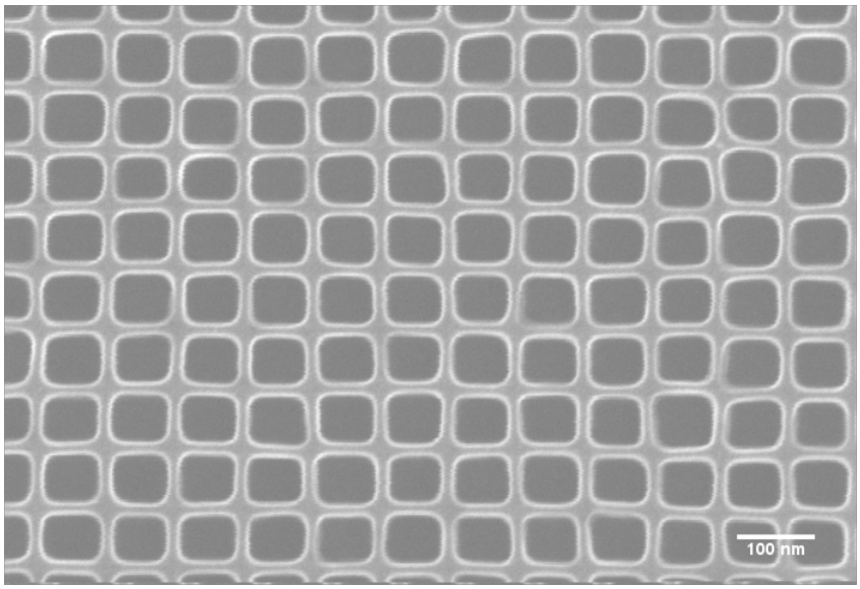

Figure 2-3: SEM image of 75nm square pattern using 60nm diameter with 90nm pitch dot pattern etching for 2 minutes, on 170nm thick PMMA layer.

The top most carbon-rich layer formed by SLIM affects the thermal properties of resist. Untreated PMMA has a glass-transition temperature of 109°C and heating patterned surface above this temperature results in resist reflow and a significant degradation of the patterns [18]. However, after the SLIM process, the samples were heated to several hundred degrees, and from our observation the quality of the patterns remained stable. An AccuThermo AW410 Rapid Temperature Processing (RTP) was used to test the heat resistant of a PMMA layer. Figure 2-4 shows the results of this thermal test. Even when the sample had been heated to 400 °C for an hour (see Figure 2-4.b), the pattern of squares remained intact and no reflow process was observed. Effectively, the structures look identical before and after heating. According to the thermal test results, we conclude that the pattern becomes heat resistant and so physical

characteristics of PMMA photo resist had changed during the SLIM process (other ways we would expect the PMMA to reflow).

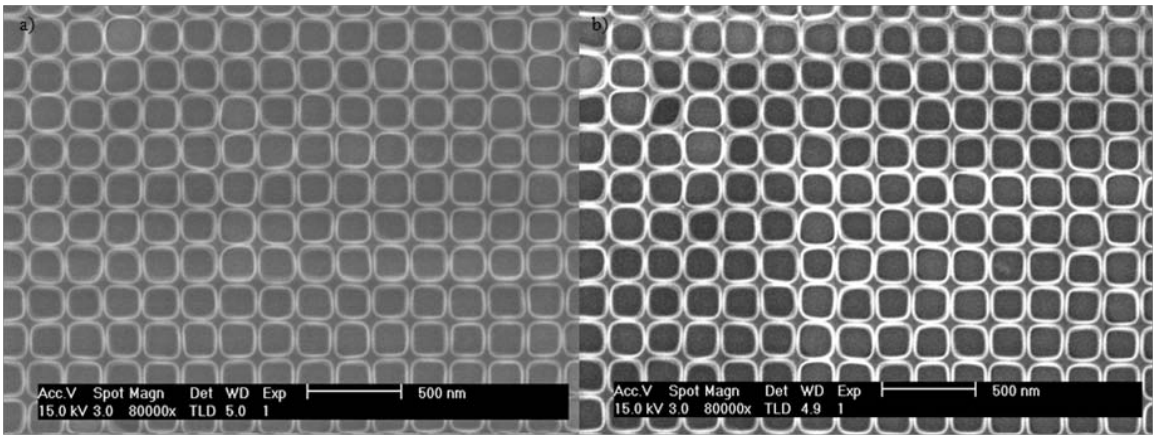

Figure 2-4: Surface carbon-rich layer increases heat resistivity. (a) An SEM image of original ~80 nm length square pattern. (b) The pattern after heating one hour at 400 °C.

2.3 Self-Limiting Ion-Milling Optimization

To investigate the details of SLIM effect, comparative experiments were carried out using 200nm pitch pattern on square grid. The precursor patterns are dot arrays of 100nm, 137nm and 175nm in diameter, fabricated on PMMA layer with the thickness of 170nm, 300nm and 450nm respectively written by a FEI XL-30 FEG Scanning Electron Microscope (SEM) equipped with NanoPattern Generation System (NPGS). The thicknesses of PMMA were measured by a Veeco Dimensions 3000 Atomic Force Microscope (AFM). Figure 2-5 shows the shapes of elements before and after argon plasma etching. The images in figure 2-5. a, c, e are the precursor dot patterns with 100nm, 137nm and 175nm in diameter, on a 300nm thick PMMA layer, while 2-5. b, d, f are their corresponding square patterns. Although the original sizes are different, the sizes of square self assembled by SLIM effect are of the same size. The final wall thickness of

nearby square pattern is about 20nm, and it does not depend on the size of the precursor pattern element. Figure 2-6 shows the pattern element size vs etch time for samples of various PMMA thicknesses. It shows that the photo resist thickness, as well as the original pattern size, also contributes to the time cost of the SLIM process, in general thinner resist requires less time to form non-circular pattern. And the result again proves the ending square pattern sizes from different samples are almost the same. Presented series of experiments support the assumption that in a SLIM process, the most important factor is the original pattern grid, the grid defines the shape, while the pitch determines the final size of formed non-circular pattern element. The original pattern size and resist thickness, however, will influence the processing time of SLIM, but not the size of the square and the wall thickness.

Pattern size distribution is a major issue of BPM fabrication. Large size distribution causes large switching field distribution [19], which influences recording quality a lot. Statistical analysis has been done on SLIM process using original dot size in 100/137/175 nm with 200nm pitch, on PMMA thickness of 300nm. Figure 2-7 shows pattern size change with etch time, as well as standard deviation. Curves in the plot show the same trend as ones in Figure 2-5, starting with different size and ending at the same value. Pattern size distribution is not high, around 2%. We can see size distribution of 175nm dot pattern curve is slightly larger than the other two curves. This is because 175nm is the largest diameter among three dot patterns with the same pitch. As a result, the comparatively closer-packed pattern got more influence from back scattering electrons which makes deviation bigger. The calculated final square pattern size demonstrates

lower distribution comparing to other patterns in the process, because the sizes are limited by SLIM effect.

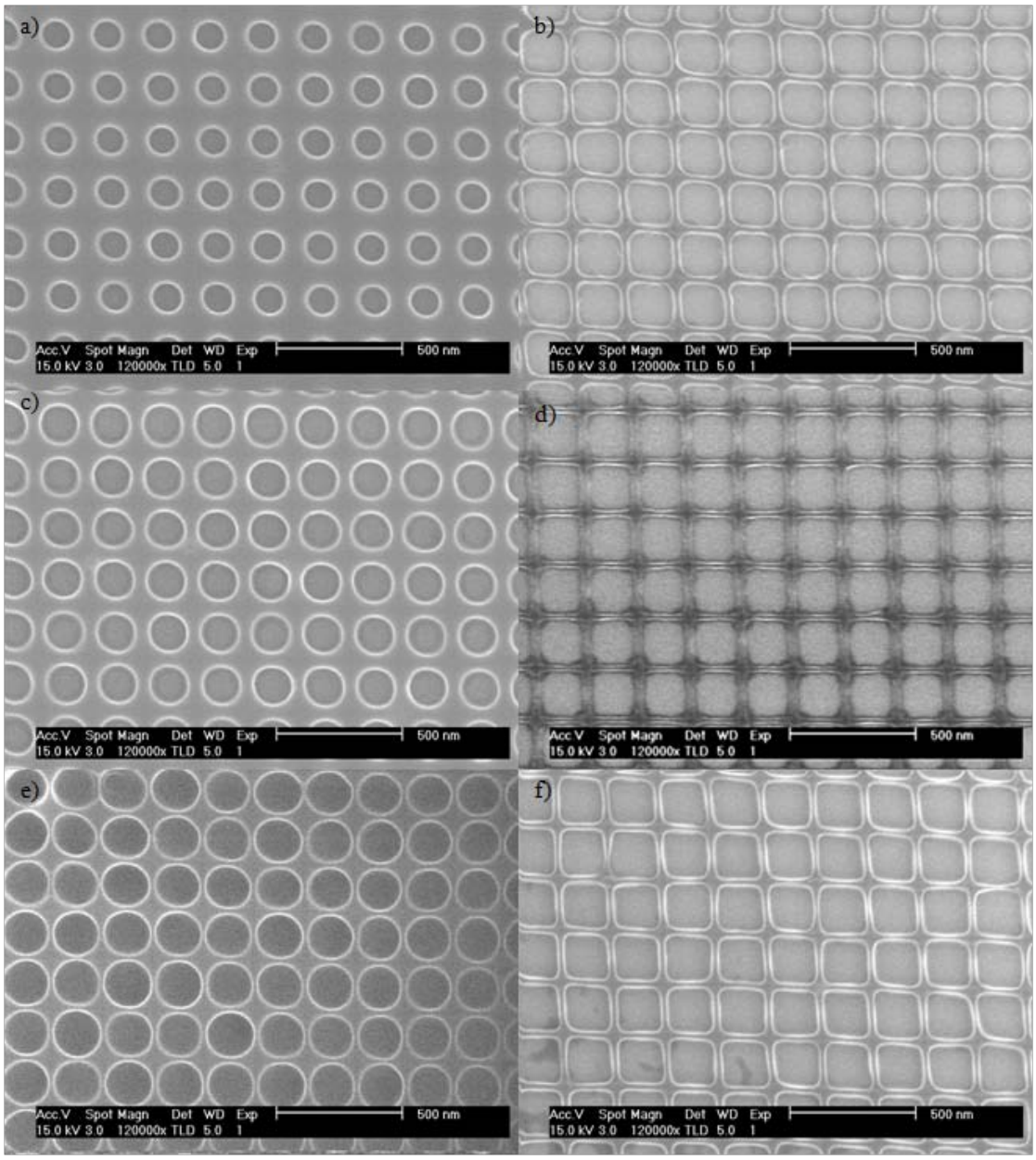

Figure 2-5: SEM images of original precursors and square patterns with 200nm pitch after SLIM. (a), (b), 100nm dot pattern with 200nm pitch and its SLIM pattern. (c), (d), 137nm dot pattern with 200nm pitch and its SLIM pattern. (e), (f), 175nm dot pattern with 200nm pitch and its SLIM pattern on a 300nm PMMA layer.

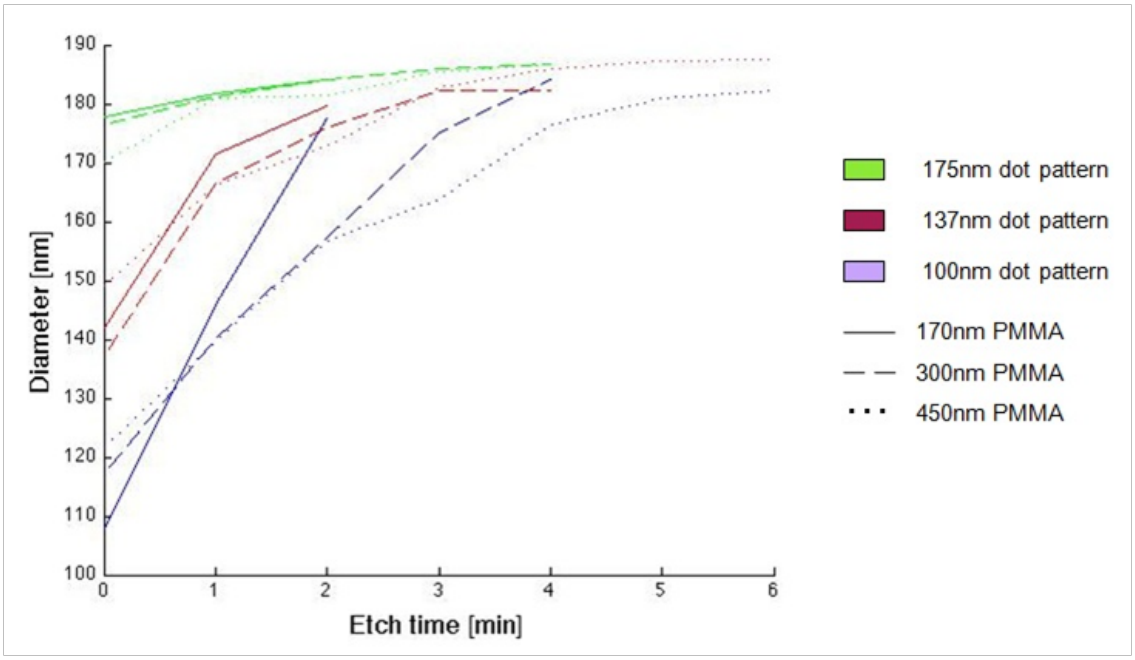

Figure 2-6: A plot of pattern sizes vs etch times for different starting size and resist thickness, interpreting the lateral etch rate in SLIM process.

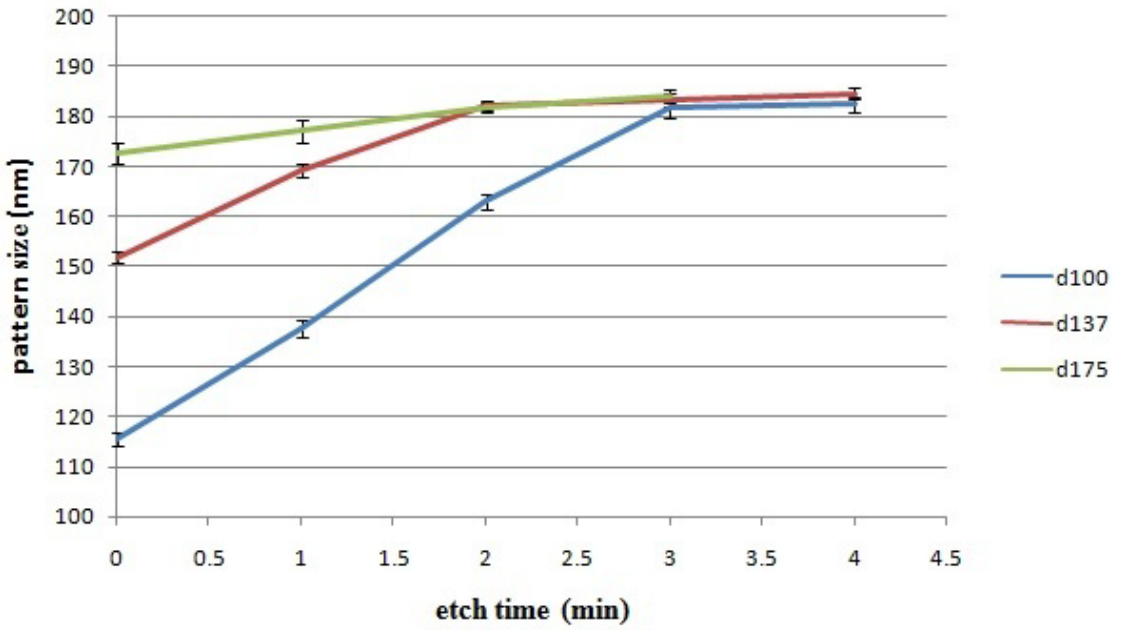

Figure 2-7: A plot of pattern size vs etch time for different starting size with error bar on 300nm PMMA layer.

Pattern squareness is calculated by dividing diagonal distance of a shape by its length. The results of the same group samples' squareness vs etch time are shown in Figure 2-8. The dash line represents perfect square, as a reference. For dot pattern with 100nm diameter, low rate of increase of squareness during first two minutes of etching indicate that wall thickness in between squares has not reached the critical value. Squareness increased a lot in the third minute for pattern change and in the last minute, since the pattern shape had already change into a square like shape, curve slope value became small again. The same process happened in the 137nm curve, only in the last minute, squareness decreased. The reason for this may be image area difference causing by exposure difference, or pattern starts to collapse because of over etching. The 175nm curve is more like a straight line, with a little change in slopes. That is acceptable because the 175nm starting size is already near the final square pattern size. Wall thickness reaches the critical value soon after the argon etching starts.

Pattern shape fitting was done by colleague in my group. Contours of the squares were fitted with the curve of the following type:

$$|x|^n + |y|^n = R^n \ , \tag{2-1}$$

where R is the half diameter of pattern being fit, parameter n describe squareness, the larger the value of n , the sharper the corners of the shape. Pattern is a circle n equal 2, and when n is infinite, pattern is infinitely close to a square. Figure 2-9 explains the algorithm of this pattern fitting investigation. The left plot is a function: $x^6 + y^6 = 1$, to give a general idea how the fitting pattern looks like. Right part of the image represents the fitting result of 175nm dot pattern being etched for 2 minutes. White contours achieved by filtering of the original image, the red ones are the fitted pattern. Cross in

the center is estimated by program pattern center. The fitting software was programmed in Python.

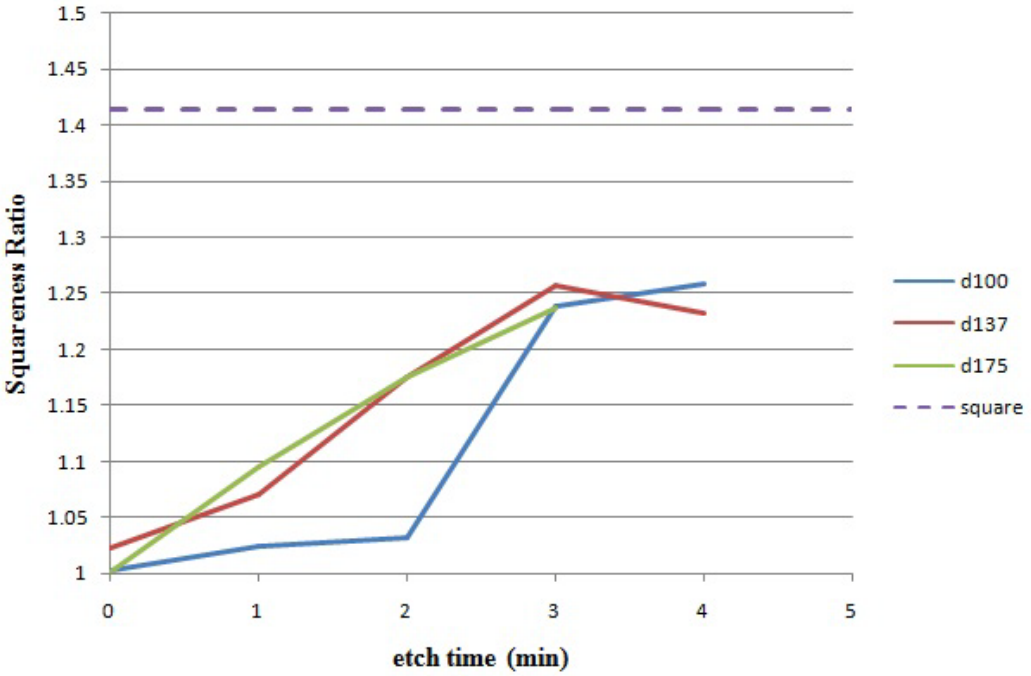

Figure 2-8: A plot of Squareness Ratio vs etch time for different starting size on 300nm PMMA layer.

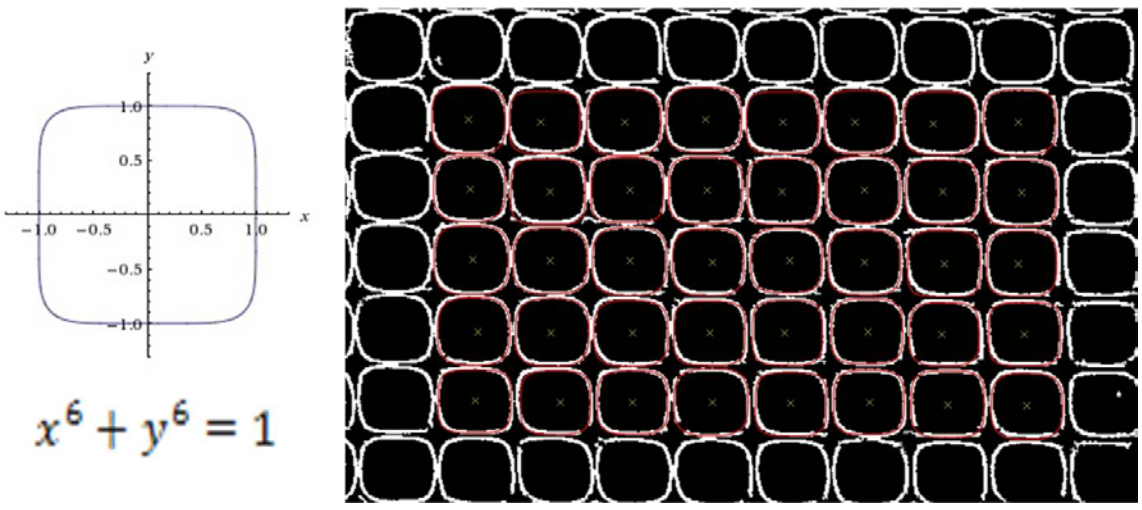

Figure 2-9: SLIM pattern fitting algorithm. White lines are filtered pattern, red lines are fitted pattern.

Fitting results n are plotted in Figure 2-10, vesus etch time. The maximum value of n is about 6.7, from 175nm dot pattern being etched for 3 minutes. 137nm dot pattern also reached n bigger than 6, while 100nm dot pattern only got n about 4.2. It appears dot pattern with 137nm and 175nm showed better squareness then 100nm dot pattern. Considering the pattern size deviation from Figure 2-7, 175nm dot pattern had larger size distribution. As a result, using 137nm dot pattern as the pre-cursor pattern is a better choice. This analysis shows that initial diameter to pitch ratio of 0.67 is favorable for SLIM process.

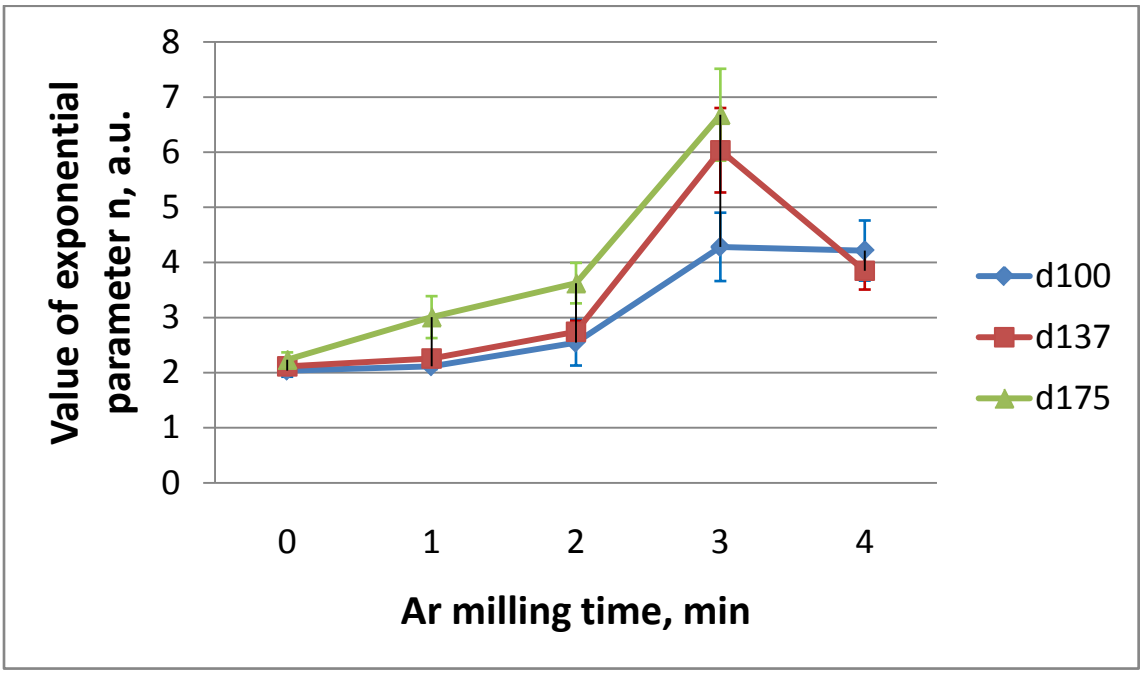

Figure 2-10: Value of fitting parameter n vs etch time.

2.3 Summary

The described SLIM approach provides a great way to overcome the difficult proximity effect problem which troubles the nanofabrication industry for decades to print non-circular patterns in small size. The precursor dot pattern can be printed by different

means of patterning, such as electron beam lithography, optical lithography and block copolymer self assembly [20]. The following argon plasma treatment enables non-circular pattern to be formed in a large area at the same time, saving time and effort from defining corner shape and compensating dose distribution from proximity effect [21]. SLIM is a low cost and more efficient way of fabricating non-circular patterns comparing to the use of e-beam lithography or other serial printing methods. It also helps to achieve close-packed small non-circular patterns which could not be realized even by expensive e-beam lithography tools.

Chapter 3: Pattern Fabrication

3.1 Introduction

SLIM process uses predefined dot patterns and argon plasma to generate non-circular patterns on PMMA. The technique is an efficient way of producing high resolution patterns on resist mask. However, to fabricate a BPM disk, pattern should be transferred from mask to magnetic layer, which involves pattern transfer and usually requires isolated pattern to be physically fabricated. In my research work, electrochemical deposition, evaporation and sputtering deposition were used for the investigation of non-circular pattern fabrication from SLIM process.

3.2 Electrochemical Deposition

Electrochemical deposition was used to deposit metallic nanostructures into SLIM formed templates. In a typical electrochemical deposition system, metal ions (e.g., Ni^{2+}) from an aqueous solution of a given metallic salt (e.g., $NiCl_2$) are deposited onto a negatively biased electrode by driving an electric current through the so-called electrochemical cell. Positively charged metal ions accept electrons from the negatively biased *working* electrode or cathode (this is referred to as a reduction reaction), while negatively charged ions of the corresponding salt (e.g., Cl^-) release extra electrons onto a positively charged *counter* electrode or anode (this is referred to as an oxidation reaction). This process is also known as electroplating [22]. It is low energy and low cost process for depositing metal on conducting surfaces. In some processes the metal anode is used as a continuing source of the metal ions that dissolves into the electrolyte to resupply the metal ions removed from the solution by deposition onto the cathode. The dissolved ions

are transported to the cathode and deposited on its surface. In another approach, a non-consumable anode such as lead is used. In this case, the concentration of metal ions in the electrolyte decreases over time, so new ions need to be replenished periodically by adding them to the solution from an external source.

Among the key issues in electrochemical deposition is surface roughness. Surface roughness if unchecked and not controlled can result in defects, especially when fabricating devices with nano-scale dimension. One approach for controlling surface roughness is to intermittently positively bias the deposition process. Although this method slows down the deposition rate, it significantly improves the quality of the deposited material.

3.2.1 Nickel Plating and Results

Computer controlled Gamry PC4/750 Potentiostat was used to conduct electrochemical experiments discussed below. This system was used to plate nickel into SLIM patterned template to form large arrays square magnetic pillars. Such device structures are of interest for applications in magnetic cellular logic. They also allow closer investigation of the morphology SLIM templates. Figure 3-1shows a schematic the electrochemical cell used in this research. The working electrode is a silicon wafer patterned using SLIM process; the counter electrode is a nickel wire. The electrodes are immersed in a nickel chloride solution, along with the reference electrode. The chemical reaction describing nickel deposition is given by the following equation

$$Ni^{2+} + 2e^{-} \longrightarrow Ni(s), \qquad (3\text{-}1)$$

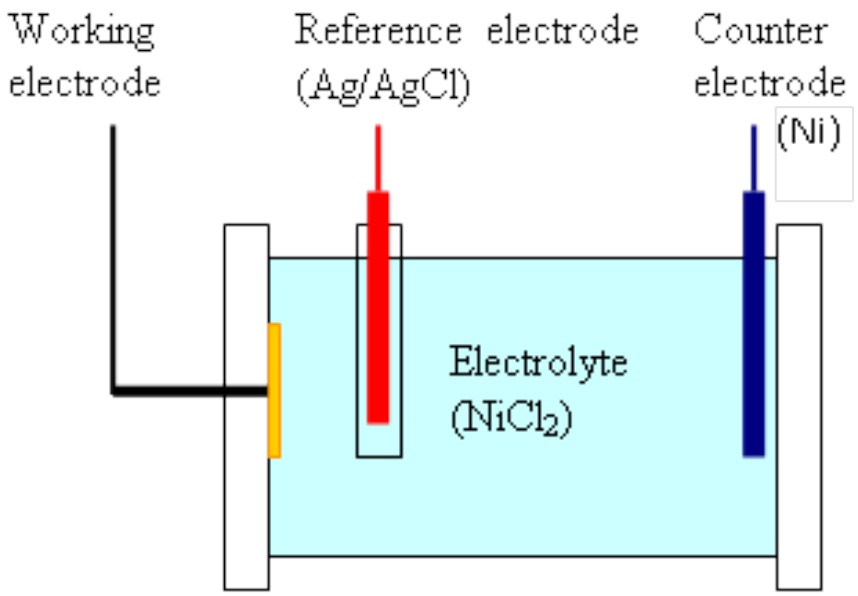

Figure 3-1: Schematic of Ni electroplating system in the project.

nickel ions in solution capture two electrons from the working electrode and become a solid nickel coated on sample. This is only half of the total reaction.The other half of the process is that solid state nickel atoms from the nickel counter electrodegets oxidized and dissolves into the electrolyte as nickel ions. In general, this electroplating reaction is consuming nickel from the counter electrode and deposited nickel ontothe working electrode (sample) [23].

Several parameters need to be controlled to optimize the electroplating process: time, concentration, and input wave function. Deposition time is calculated as

$$t = (d \times \rho \times F \times n)/(J \times M), \quad (3\text{-}2)$$

where d is the depth of plating; ρis the density of Ni, which is 8.9g/cm^3; F is Faraday's Constant, which is 96488C/mol; n is the number of electrons in reaction, which is 2; J is current density; M is molecular weight of Ni, which is 58.72g/mol. Substituting all the values into the equation above gives, deposition time as 10^{10} ×d ×J-1 level. During the experiments, deposition area could not be reliably controlled because of defects on

sample. We used the patterned area of 6,000 um^2 and the deposit depth of ~200 nm, which gives the electroplating time in tens of seconds range.

An n+-doped Si (100) wafer was used as the substrate. The wafer was dipped in 10% buffered hydrofluoric acid (HF) to remove the oxides on the surface, followed by rinsing with deionized water. Melted indium metal was spread on the bottom of Si wafer, and baked on a hot plate at 200ºC for 15 minutes. The baking process made the melted indium penetrate into the wafer and changed the apparent resistance of the silicon from the order of mega-ohms to tens of ohms. 5 nm of tantalum (Ta) was sputter deposited onto the wafer as an adhesion layer. 10 nm of palladium (Pd) was sputter deposited onto the Ta adhesion layer as a seed for electrochemical deposition. This was followed by spin-coating of PMMA of ~350nm thickness and patterning of PMMA using e-beam lithography. Following the deposition of nickel into the openings in PMMA, the PMMA can be stripped by a 10 minute oxygen plasma etching process. With careful control of processing time, nickel pillars can be obtained.

A number of experiments using dot array pattern were conducted to optimize the concentration, input wave function, and deposition time. Figure 3-2 shows selected results. At -1000mV DC wave input and deposition time of 20 seconds in 0.75 M solution, there was no pillar formed with very poor resulting uniformity of deposited device structures (Figure 3-2. a). In Figure 3-2. b, c the square wave input centered at -675 mV with 325 mV amplitude at frequency of 10Hz was used with the deposition times of 6 minutes and 12 minutes, respectively, in 0.1 M solution. Even after such a long time deposition time, there was no pillar formed, suggesting that 0.1 M solution was too dilute. In Figure 3-2. d, e and f, the same square wave input was used with 0.75 M solution and

deposition times of 60 seconds, 90 seconds, and 120 seconds. In 3-2. d there are little mountains formed, in 3-2. e good quality cylinders are formed, most of them have flat top while some have a sharp tip, in 3-2. f almost all the pillars appear the same, the tops are smooth, height is about 350 nm, which is just about the thickness of the PMMA layer. These results show that the best settings for Ni electroplating include a square wave input function [24], shown as Figure 3-3, centered at -675 mV with 325 mV amplitude at frequency of 10 Hz, solution concentration of 0.75 M, and deposition time of 1 ~ 2 minutes depending on the depth of deposit.

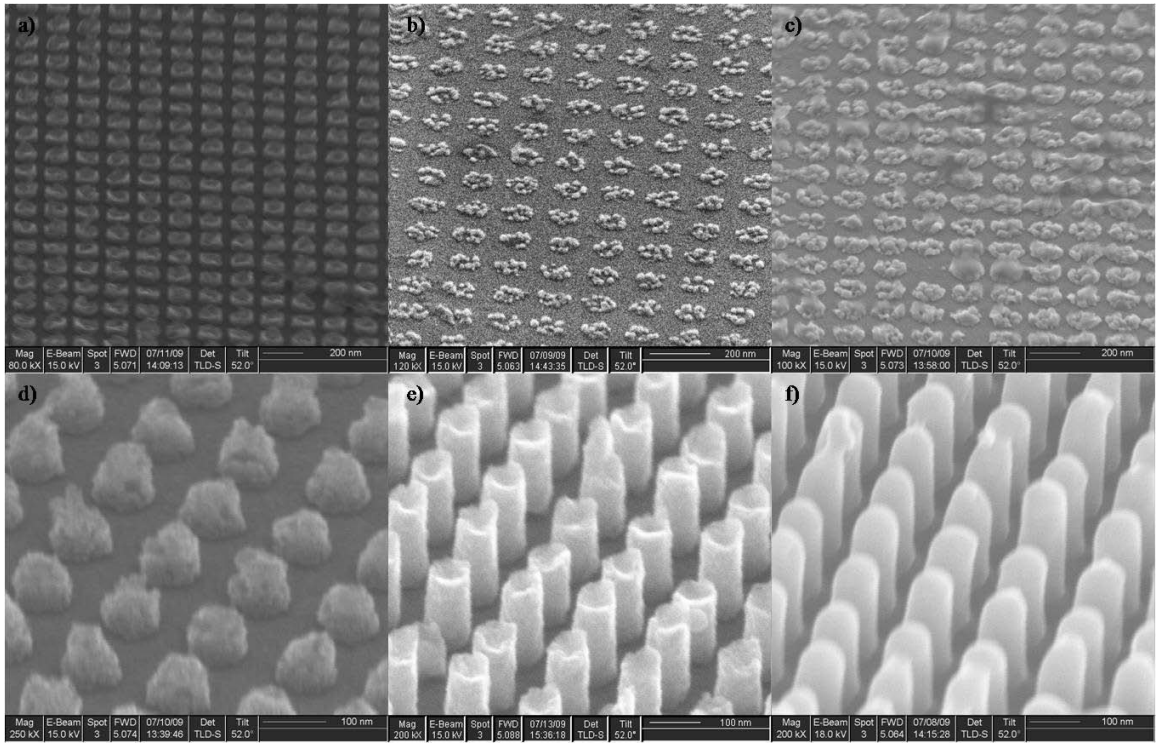

Figure 3-2: (a) DC input with -1000mV, 20 sec in 0.75 M solution. (b) Square wave with -1000mV/-350mV, 10Hz, 6 min in 0.1 M solution. (c) Square wave with -1000mV/-350mV, 10Hz, 12 min in 0.1 M solution. (d) Square wave with -1000mV/-350mV, 10Hz, 60 sec in 0.75 M solution.

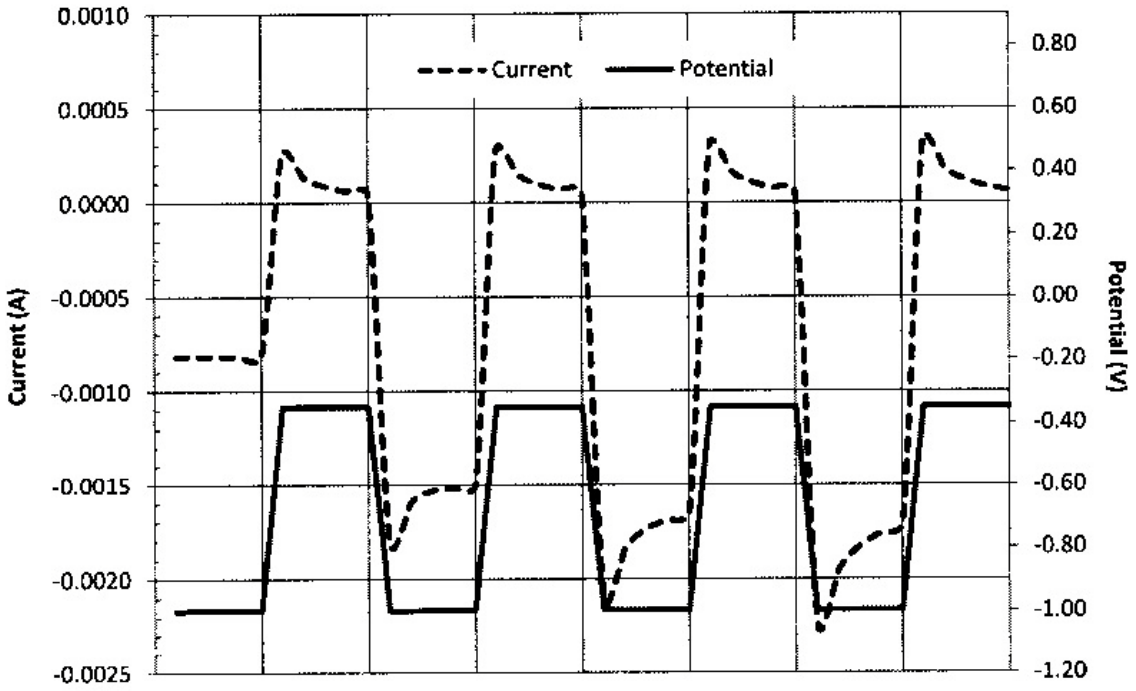

Figure 3-3: Input square wave function and the corresponding current.

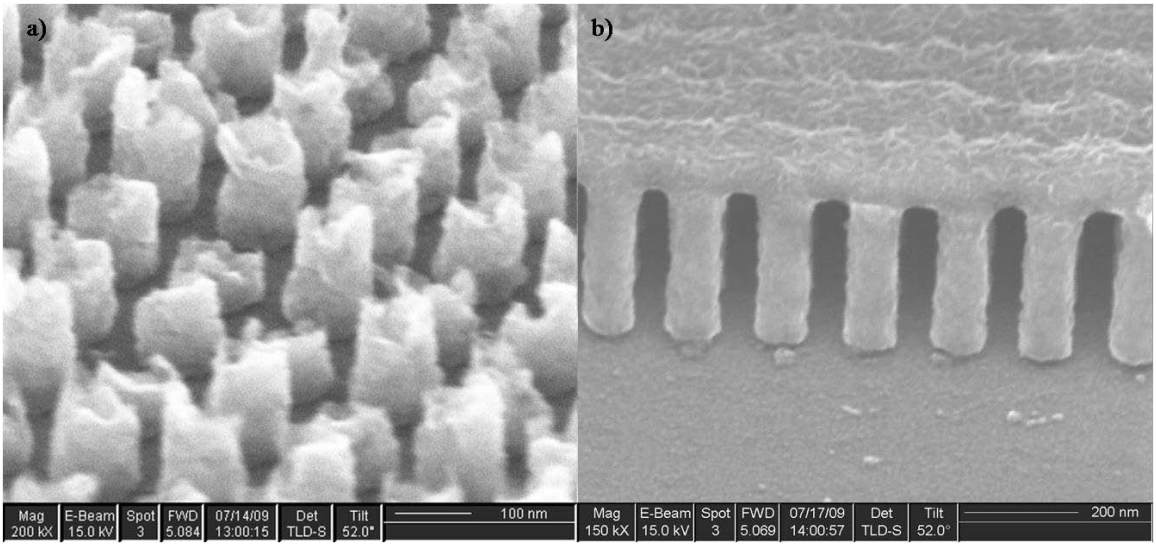

Figure 3-4: (a) Nickel pillars collapse after over electroplating. (b) The over deposited layer stays intact after resists stripping by oxygen plasma. Well-defined nickel pillars can be seen.

Over-plating is a convenient way to investigate internal structure of patterns. Figure 3-4. a shows the Ni structures after oxygen etching, where nickel pillars collapse and randomly breaking off the wafer surface. Figure 3-4. b shows the over-plated deposited layer, which stays intact after oxygen etching. Disregarding the top over-plated cover, the nickel pillars high light the internal details of the pattern.

Next, nickel was electroplated into SLIM formed templates. The process schematic is shown in Figure 3-5. Although most aspects of the processing remain the same, some differences are apparent. According to the ~ 35 nm/min etch rate, the depth of pattern should be ~ 200 nm when squares are formed. That depth requires a 1 minute deposition in a 0.75 M solution. However Figure 3-6. a shows a well formed square pattern with ~125 nm length. Figure 3-6. b shows the result of 2 minute deposition in a 0.75 M solution using a square wave input. It is found that even after 2 minutes, the patterns are still not filled up with nickel, while the top of walls between nearby squares have already been covered by nickel layer. The reason for this phenomenon, which is discussed in chapter 2, is the dramatic change in the composition of PMMA due to argon milling. The newly formed carbon rich layer on PMMA surfaces become conductive [25, 26], thus nickel coats the wall of the pattern rather than filling the pattern from bottom up. This property of the SLIM fabrication templates makes electroplating into SLIM square patterns significantly more challenging.

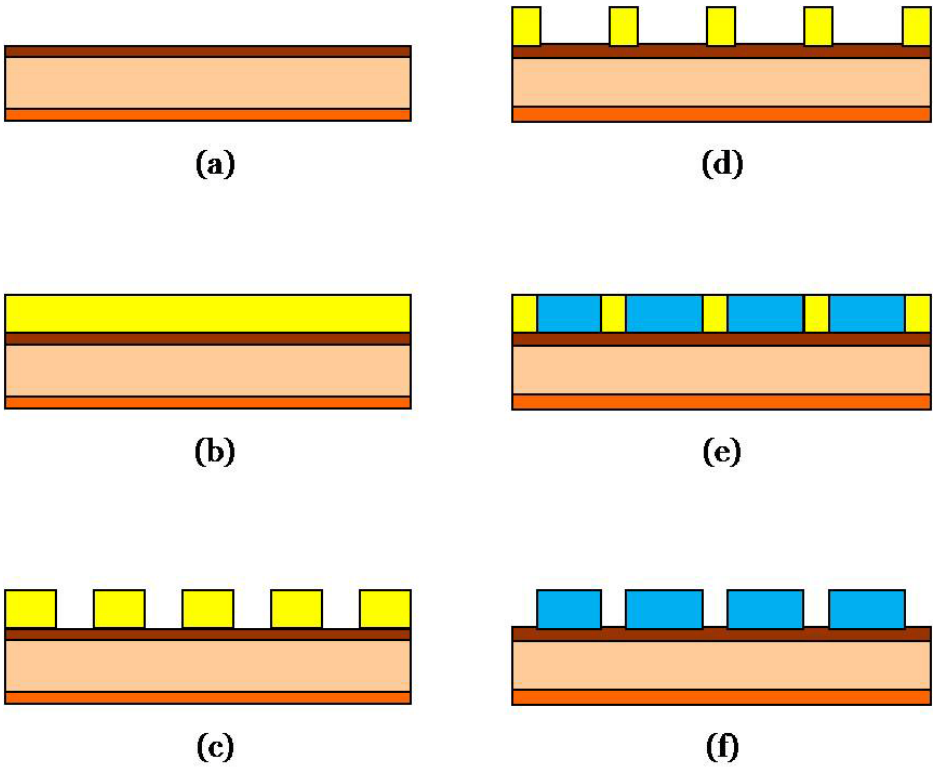

Figure 3-5: Process Schematic: (a) Sputter deposit 5nm Ta and 10nm Pd on the wafer. (b) Spin-coat 350nm PMMA. (c) E-beam lithography patterning. (d) Argon etching process. (e) Electroplating nickel. (f) Oxygen cleaning etching to remove PMMA.

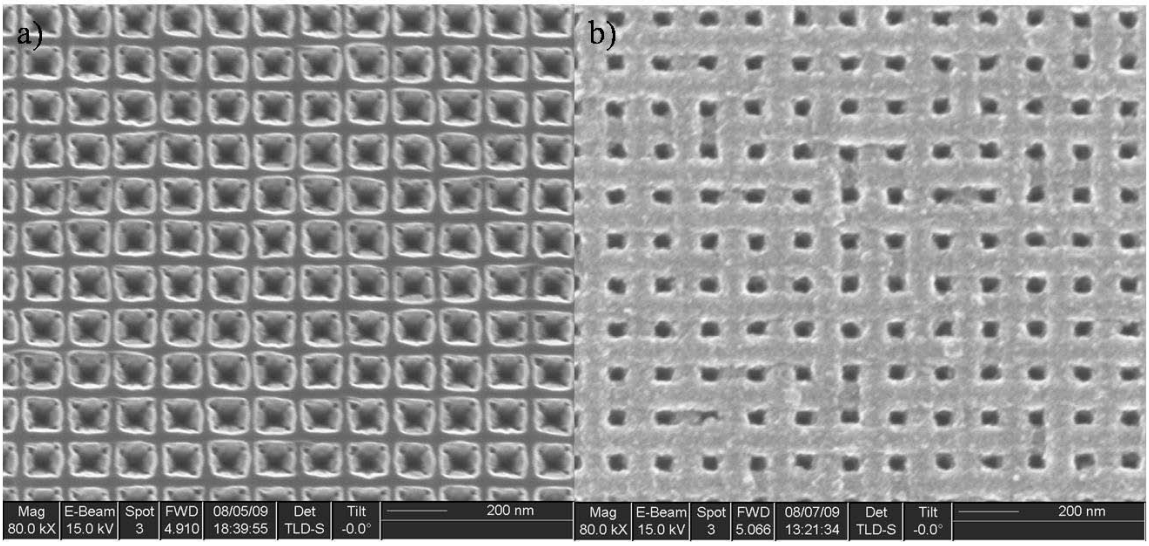

Figure 3-6. (a) Prepared square patterns of ~ 125nm length and 150nm pitch. (b) After 2 min depositing in 0.75 M solution, square wave input.

Figure 3-7 shows well packed nickel pillars in a SLIM formed template. Figure 3-7. a shows a 52 degree angle view of 80nm square nickel pillars formed by nickel chloride electrochemical deposition. Also from Figure 3-7. a the indent in the center of each Ni pillar can be observed, the possible reason for this phenomenon is the dramatic change in the composition of PMMA due to argon etching. The newly formed conductive carbon rich layer on PMMA top surfaces makes nickel coat the wall as well while filling the pattern from bottom up. When lift off, brisk bridge was washed away by ultra sonic bath. This is why we can still find some tips on the top edge of square pillars. An additional argon milling with all the settings kept as in prior experiments was run on the sample. Because of the slow etch rate, the argon etching shallowly shaves the top of the square patterns, making the surface flat while not decreasing the pillar height much. Figure 3-7. b is the resulting pattern shape after the argon milling, well packed square pillars with high spatial resolution can be observed.

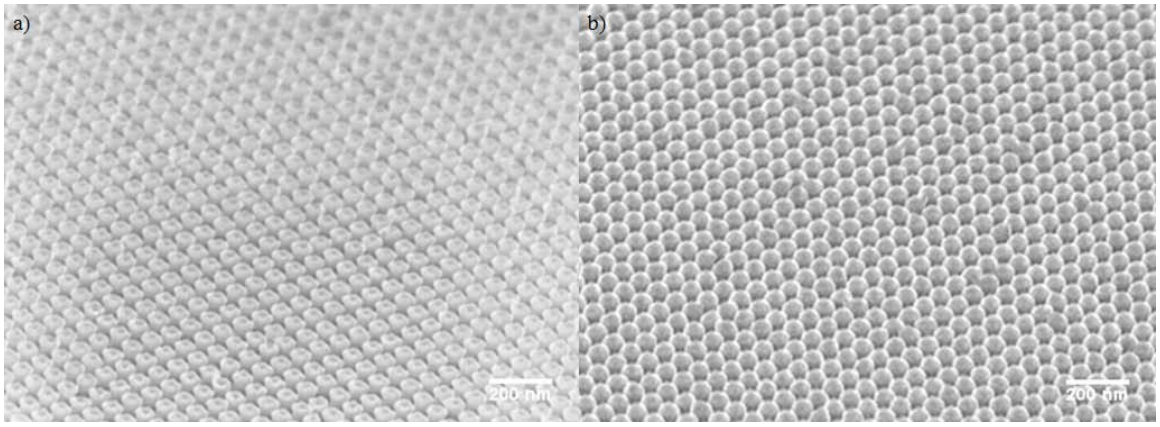

Figure 3-7: Electrochemical deposition in square patterns. (a) 52 degree angle view of 80nm nickel square pillars formed by electrochemical deposition. (b) A 52 degree view of square pillars with flat top surface after argon plasma treatment.

3.2.2 Permalloy Electrochemical Deposition

Permalloy (Ni80Fe20) was selected as metal material of electrochemical deposition [27] as well, because it is a common “soft” magnetic material (with a low coercivity). The solution is made up of several different solvents, with their concentration as follows: 110 g/L $NiCl_2 \cdot 6H_2O$, 1.8 g/L $FeCl_2 \cdot 4H_2O$, 25 g/L H_3BO_3, 0.01 g/L sodium dodecyl sulfate (SDS) and 0.12g/L M Saccharin. The PH value of the solution is controlled to be 2.95, and the working voltage is 0.914V. Among the above solvents, $NiCl_2 \cdot 6H_2O$ and $FeCl_2 \cdot 4H_2O$ contribute Ni and Fe, H_3BO_3 controls PH value, SDS and Saccharin are additives helps to control the deposition process better [28]. Figure 3-8 shows the result of permalloy electrochemical deposition after argon milling to shave the top surface. The fabricated patterns are similar as the ones from nickel deposition.

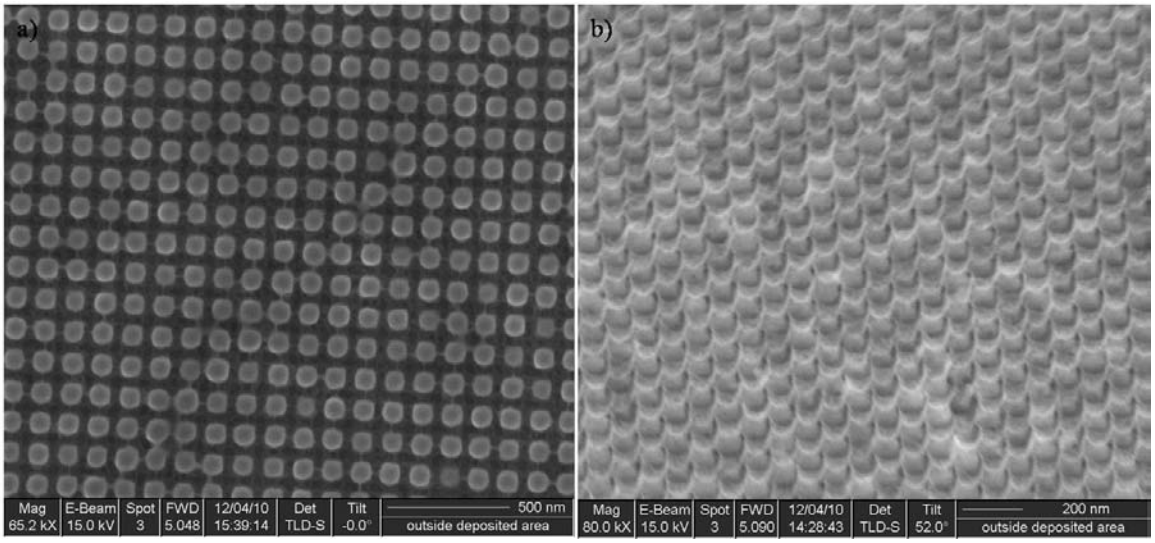

Figure 3-8: Permalloy electrochemical deposition in square patterns with argon milling treatment. (a) 52 degree angle view of 80nm permalloy square pillars formed by electrochemical deposition and argon treatment. (b) A 52 degree view of square pillars with flat top surface by argon plasma treatment.

3.3 Evaporation Deposition

Electrochemical deposition is a good way of depositing particular metal layers onto substrates with constant area and resistivity, in order to keep control of the process. However, in my experiment in SLIM, these parameters are difficult to be reproduced exactly the same. That is why we need to find some new approach to do metal deposition.

3.3.1 Thermal evaporation

Evaporation is one of the most popular ways of thin film deposition. Thermal evaporation uses a high current to heat evaporation source, evaporates it and makes the source particles go directly to the sample target. The key points of evaporation deposition are vacuum, distance and sample surface roughness. In a high vacuum circumstance, particles will not collide with each other and attach to target directly. The absence of background gas such as oxygen will also avoid reactive action between particles, for example, aluminum evaporated in oxygen will produce aluminum oxide. The distance between source and sample influences depositing rate and thin film purity, usually the smaller distance is better. Sample surface roughness is related to thin film surface roughness, because the evaporated particles arrive at the sample at almost the same incident angle, the thin film formed basically duplicates the substrate surface profile. Substrate surface roughness can be controlled by depositing a metal seed layer like Tantalum (Ta).

The thermal evaporation system used in my project is built by students from another group, the base pressure is 2.0×10^{-5} Torr and the distance between evaporation source and sample target is about 20 cm. The source used in evaporation experiment is permalloy pellets pursuit from industry. Rate monitor is installed inside the system to

control deposition rate. The dot array pattern was first tried in evaporation experiments, Figure 3-9 shows a 55nm thick permalloy dot array pattern fabricated by thermal evaporation. Figure 3-9. a is the cross section of the pattern right after evaporation. We can see there are links between nearby patterns because of permalloy particles arriving sample target uniformly during the process. This phenomenon makes it important to control the deposit layer thickness to coordinate the pattern depth and link bridge thickness. Figure 3-9. b is how the pattern looks like after an ultra-sonic acetone bath. Obviously, the weak links were shaken off and dot patterns are isolated from each other. The problem of ultra-sonic bath operation is that it broke the link bridges by force, which makes the surface of dot pattern not smooth. We can see there are side wall on top of each pattern, left from the link bridge.

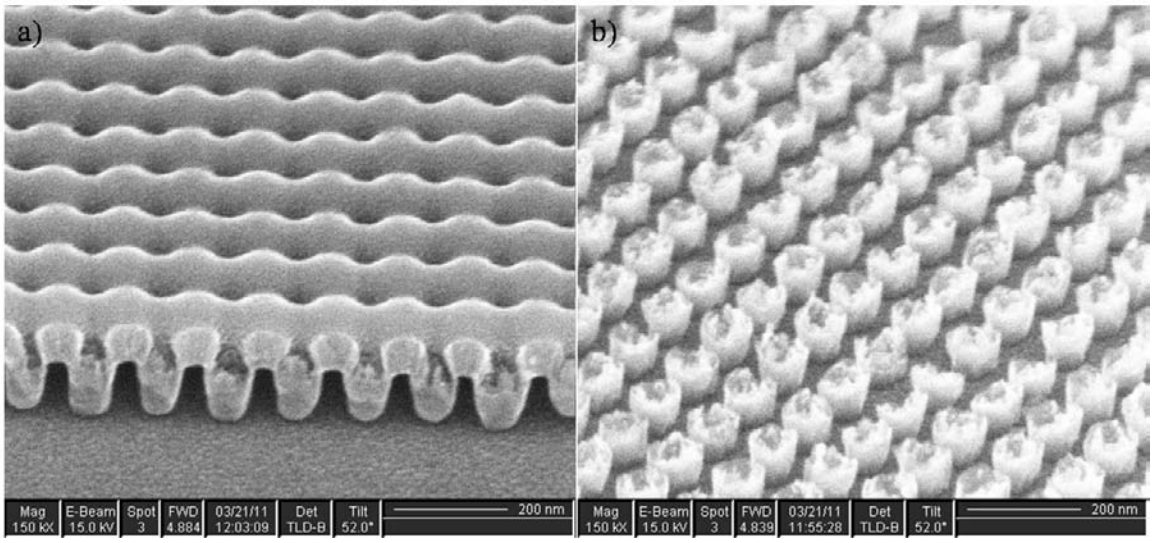

Figure 3-9: Permalloy thermal evaporation pattern. (a) Cross section of 55nm thick permalloy pattern after thermal evaporation (b) A 52 degree view of thermal evaporated permalloy pattern after acetone ultra-sonic bath.

Although with the problem of link bridges, an advantage of evaporation deposition compared to electrochemical deposition on non-circular patterns from SLIM process is that it does not have side wall coating problem. Figure 3-10 is a ~ 120nm square pattern

produced by thermal evaporation on a SLIM operated resist mask, followed by ultra-sonic bath and extra argon milling to shave sample surface. From the pattern top view shown in 3-10. a, we can see square patterns are well close-packed together, there are still side walls on top but not that high (according to the contrast compared to the center area), and from the side view shown in 3-10. b, we can see clearly that the side wall problem has been compromised although there are still some sharp tips. Also the square patterns are close-packed, but isolated from each other.

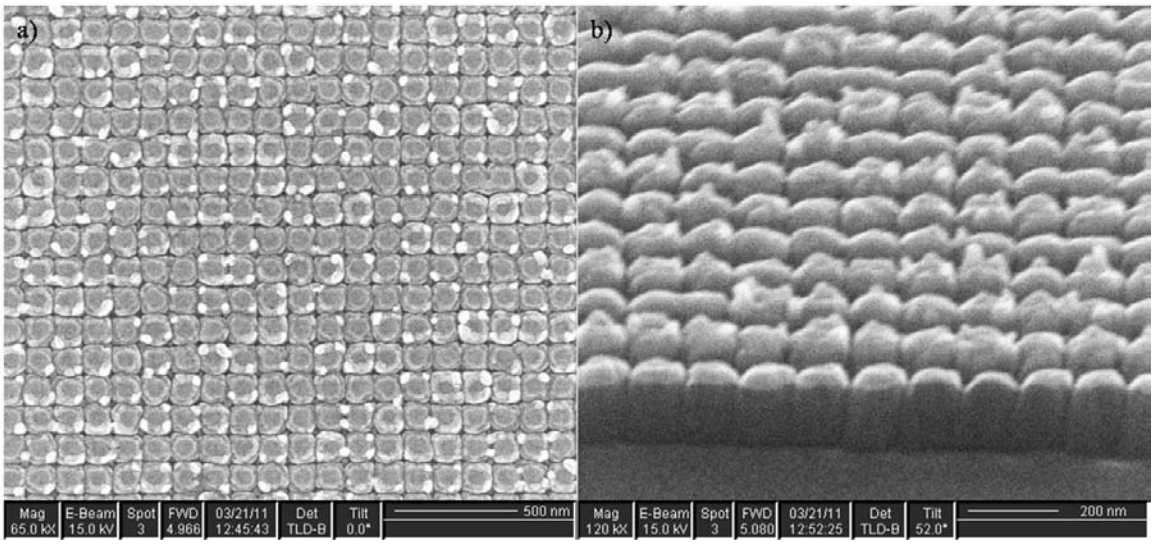

Figure 3-10: Permalloy thermal evaporation pattern. (a) Top view of 120nm square pattern after argon milling. (b) A side view of thermal evaporated square permalloy pattern after argon milling.

3.3.2 Electron beam evaporation

Electron beam evaporation is mostly the same as thermal evaporation but has a different way of heating source material. As shown in Figure 3-11, in an e-beam evaporator, filament is under source crucible rather than connect with it. Heated filament generates an electron flux, which will be guided by a magnetic control to target on source material. This configuration helps to protect the filament from being contaminated. The

detoured electron beam strikes source material, produces high temperature by kinetic energy conversion, to evaporate the source material. Since electron beam focuses on a single point, the heat on that point can be extremely high. In this case, electron beam evaporation can use materials with higher evaporation points than traditional thermal evaporation. And the exposed small area also contributes to less material consumption.

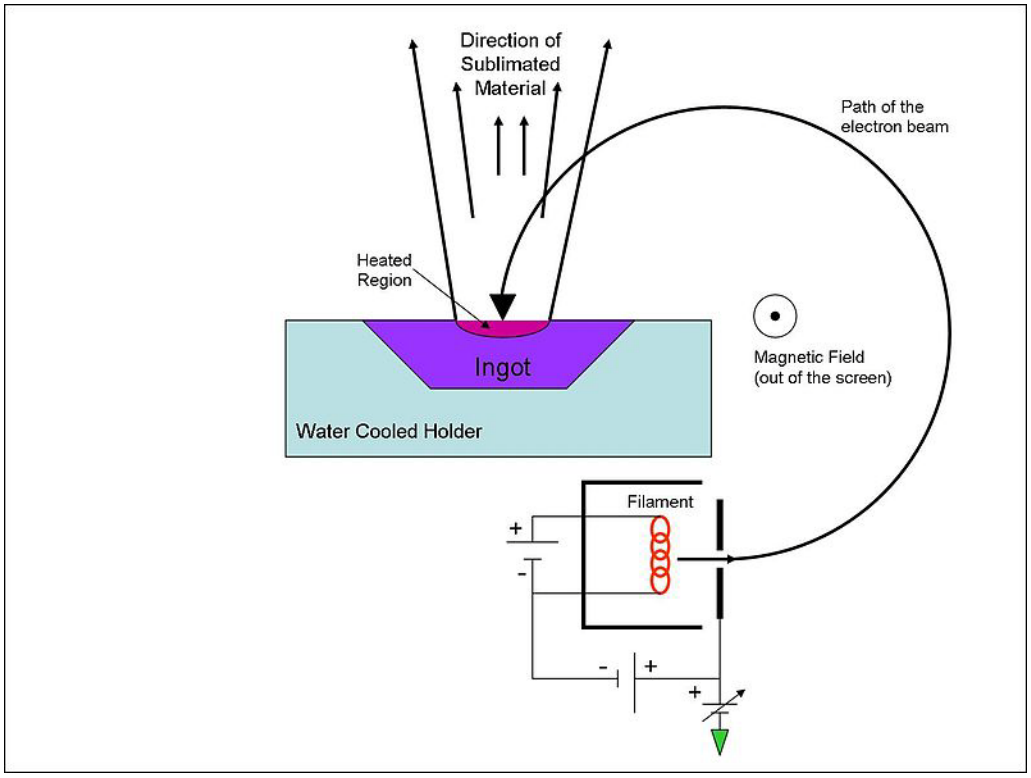

Figure 3-11: A sketch of mechanism and working theory of e-beam evaporator.

The system used in electron beam evaporation is Thermionics e-Beam evaporator, built in our clean room for quicker pumping and less dust and water vapor. The material source is still permalloy, the same as used in thermal evaporation. Base working pressure is 2.0×10^{-5} Torr, deposition rate is recorded by crystal monitor inside. By controlling the evaporated material thickness and the following argon milling time, well defined non-circular pattern can be obtained. Figure 3-12 shows a 100nm wide permalloy square

island, with a thickness of 50 nm on top of 3 nm Chromium (Cr), a seed layer suitable for evaporation (Ta is too difficult to be evaporated).

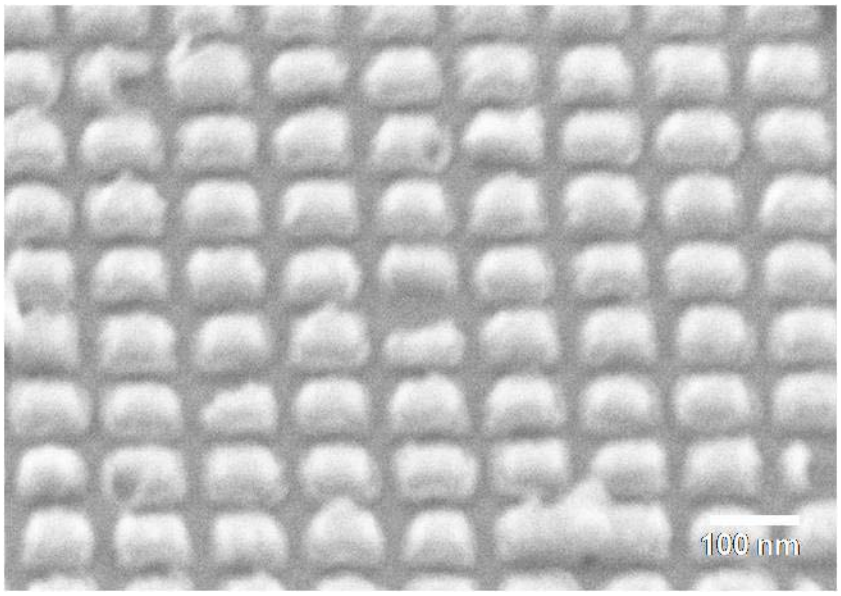

Figure 3-12: 100nm wide permalloy square pattern fabricated by e-beam evaporator.

Evaporation is convenient for thin film deposition, and the fabrication results shown the possibility of producing non-circular pattern with evaporation deposition. However, the technology has a limitation of source material. Materials such as Cobalt, Palladium and Tantalum, which are common ones used for recording media, have difficulty in being evaporated. As a result, to apply SLIM in magnetic recording media, we should use some other fabrication techniques.

3.4 Sputtering Deposition

Sputtering deposition is another physical way of thin film deposition. It uses gas (like argon) particles to strike source target, the kinetic energy from these incoming gas particles will be transferred inside source material and eventually sputter surface atoms out. These atoms will then bombard and deposit themselves onto the sample surface.

The sputtering system used in deposition experiments is an AJA UHV six-source sputtering system. The sample holder can rotate at 100 rotations per minute to keep deposited thin film uniform. The thin film receipt in this experiment is $(Co3Å\ Pd7Å)_{10}$/Ta 3nm, on top of a 10nm Ta seed layer [29]. Figure 3-13 shows a ~200nm non-circular island pattern fabricated using sputtering deposition. From 3-13. a, we can observe that although the pattern is non-circular, it is not very square, this may related to the rotating sample holder and 13nm thin film. 3-13. b shows the surface of non-circular islands are not as rough as the patterns made before with other techniques, this is because the 13nm thin film deposition makes side wall deposition and link bridge between nearby pattern very weak and could be lift off much easier. In order to optimize the sputtering deposition process, PMMA thickness should be controlled, since the layer thickness is already fixed. Thinner PMMA means better pattern transfer but stronger side wall, while thicker PMMA stands for easier lift off but lower corner resolution.

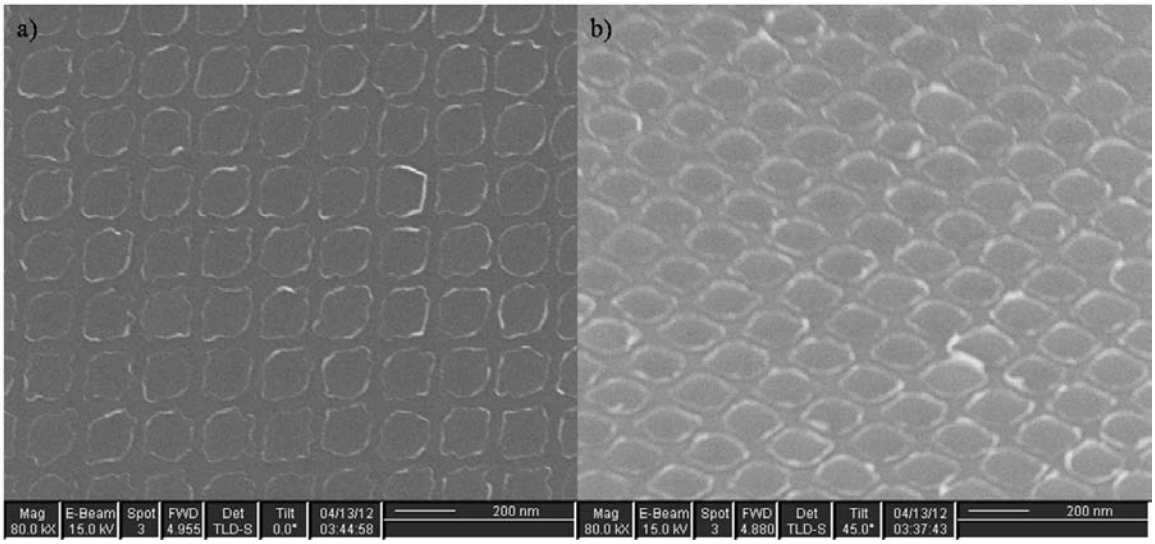

Figure 3-13: 200nm non-circular CoPd multilayer pattern fabricated by sputtering deposition. (a) Top view of the non-circular pattern. (b) A 45 degree angle view of the pattern.

3.5 Summary

In this chapter, different materials and different deposition ways were tried to fabricate close-packed non-circular patterns. The results are convincing but not perfect. Electrochemical deposition is difficult to control unless the samples have uniformed area and resistivity. Evaporation has a limitation of source material and difficulty in depositing multilayer, while sputtering deposition has corner resolution issue due to the spinning sample holder. All of the above methods suffer from side wall deposition and top links between nearby patterns. The lift off problem is a key in physical fabrication of non-circular pattern, it brings pattern non-uniformity and increases the size and shape distribution, which are major problems in BPM fabrication.

Chapter 4: Master Production Techniques

4.1 Lithography Techniques

Electron beam lithography is the most popular way of fabricating nanostructures because of its high resolution and accuracy. But the major problem of EBL is that it is a serial printing technique, the electron beam exposes desired area spot by spot, which means EBL is comparatively a slow way of printing nano-patterns. That is why it is mainly used in research and mask fabrication. For the future application in BPM or other fabrication process, SLIM should be combined with other lithography techniques to produce close-packed non-circular pattern in large area. The three promising candidate approaches are block copolymer self assembly, nanoimprint lithography and ion beam proximity lithography (IBPL). Research work has been done on nanoimprint lithography template fabrication and IBPL mask fabrication.

4.2 block copolymer self assembly

Block copolymers have been a hot topic in nano-fabrication for decades because of the self assembly property. By controlling essential parameters like molecular weight, volume fraction of the component, and the degree of segment incompatibility, block copolymers will self organized into a variety of different ordered nanostructures, such as spheres, cylinders and other complex nanostructures, as shown in Figure 4-1. This block copolymer self assembly approach is of particular interest in nanotechnology industry, since it can generate controlled high resolution nano-patterns in large area with low cost. However, there are still major problems like pattern misplace and pattern size limit to be solved before the real application in industry production.

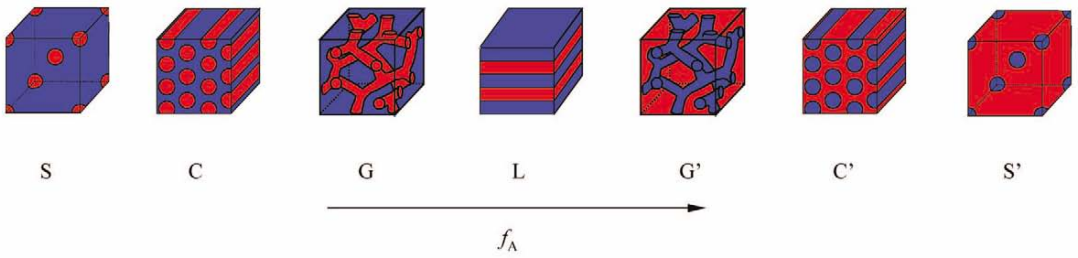

Figure 4-1: Mean-field prediction of the thermodynamic equilibrium phase structures for conformationally symmetric diblock melts. Phases are labeled as: L (lamellar), C (hexagonal cylinders), G (bicontinuous cubic), S (body-centered cubic spheres). fA is the volume fraction [30].

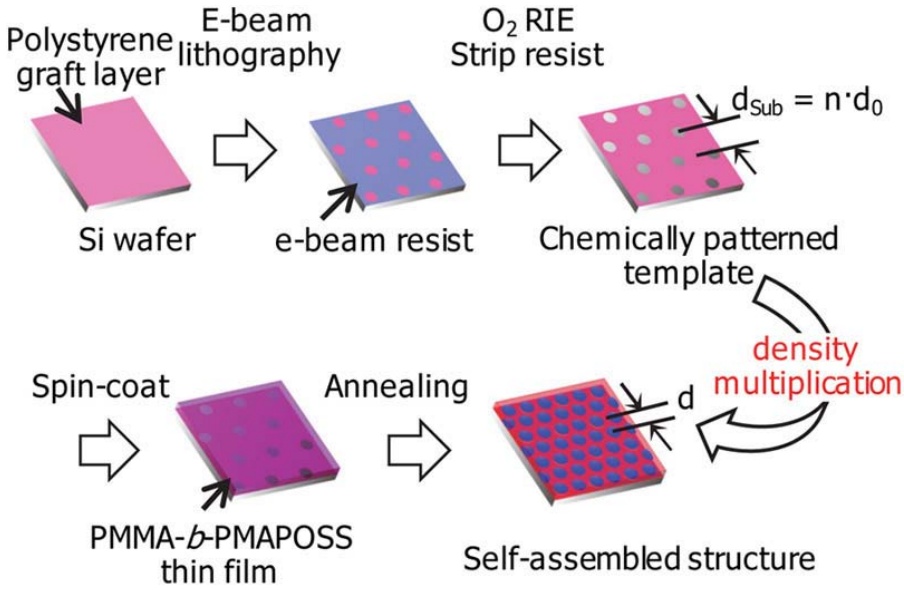

Figure 4-2: Using electron beam directed block copolymer self assembly to fabricate pattern with multiple density [31].

Directed Self Assembly (DSA) of block copolymer is improvement based on block copolymer self assembly [32]. The approach uses a defined mask of pattern with larger pitch to help generate pattern with higher density. Figure 4-2 shows a sketch of DSA operation process. An electron beam defined mask is put on polystyrene graft layer on a Si wafer, followed by a spin-coated PMMA-*b*-PMAPOSS thin film. The sample is then self assembled into a much higher density pattern by thermal annealing at 150°C or

solvent annealing in a neutral solvent atmosphere, using a vapor of carbon disulfide/acetone. The electron beam defined mask is the essential part in DSA because it directs the future self assembly of block copolymer. It solves issues like pattern misplace and pattern size but leads to new problems like mask resolution and pattern transfer.

According to SLIM theory, argon ions strike the resist surface, depleting the oxygen and hydrogen out, making the surface carbon-rich to protect itself from further etching. This theory should work on any resist that made up of carbon, oxygen and hydrogen, so there is a high possibility that SLIM effect is able to happen on block copolymers. To apply SLIM process in directed self assembly of block copolymer, future investigation is needed.

4.3 Nanoimprint Lithography

Nanoimprint lithography is another efficient lithography with low cost and high throughput [33, 34]. It generates pattern on resist by mechanically deformation of imprint resist and subsequent processes. As shown in Figure 4-3, a well patterned master mold can duplicate hundreds of daughter molds, and each daughter molds can again produce hundreds of patterns sample. The imprint resist is usually a monomer or polymer formulation which is cured by heat or UV treatment during pattern transfer. This technique is suitable for nano-patterning master production in industry. The key challenges are the master mold fabrication and imprint resist viscos, which can cause contamination on molds and damage on patterns.

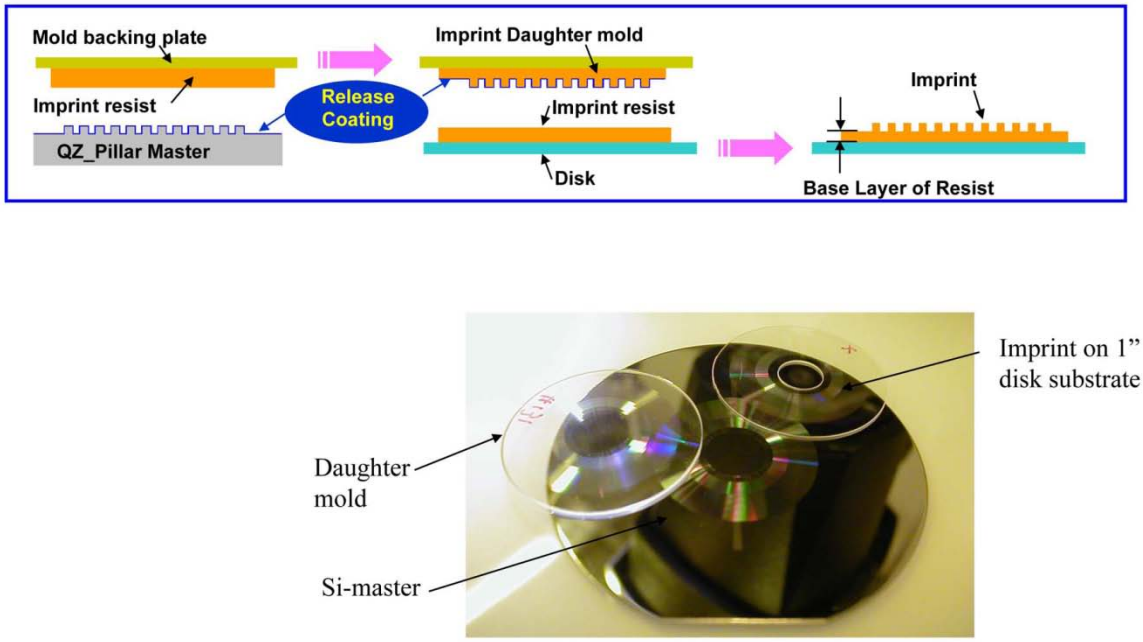

Figure 4-3: Nanoimprint lithography flow chart and sample of imprint templates.

For the purpose of future application in fabrication industry, the combination of SLIM process and nanoimprint lithography seems a promising route for the master production of non-circular patterns. An experiment of fabricating a nanoimprint mask of non-circular patterns was run to prove the possibility. SiO_2 was chosen as the nanoimprint mask material. A 300nm PMMA layer was spin-coated onto a SiO_2 wafer, followed by e-beam lithography to define precursor dot pattern. 120nm wide square pattern was generated by a SLIM process argon etch, the pattern is then transferred into SiO_2 layer by a 100W CHF_3 etch [35], for about 5 minutes. The carbonized PMMA residue was removed by oxygen cleaning in RIE system. The transferred square pattern is shown in Figure 4-4. 120nm wide square was successfully transferred but some corner resolution loss could be observed. This experiment proved fabrication of non-circular pattern mask using SLIM process for nanoimprint lithography is feasible. The process could be optimized in future to get better pattern transfer and higher corner resolution.

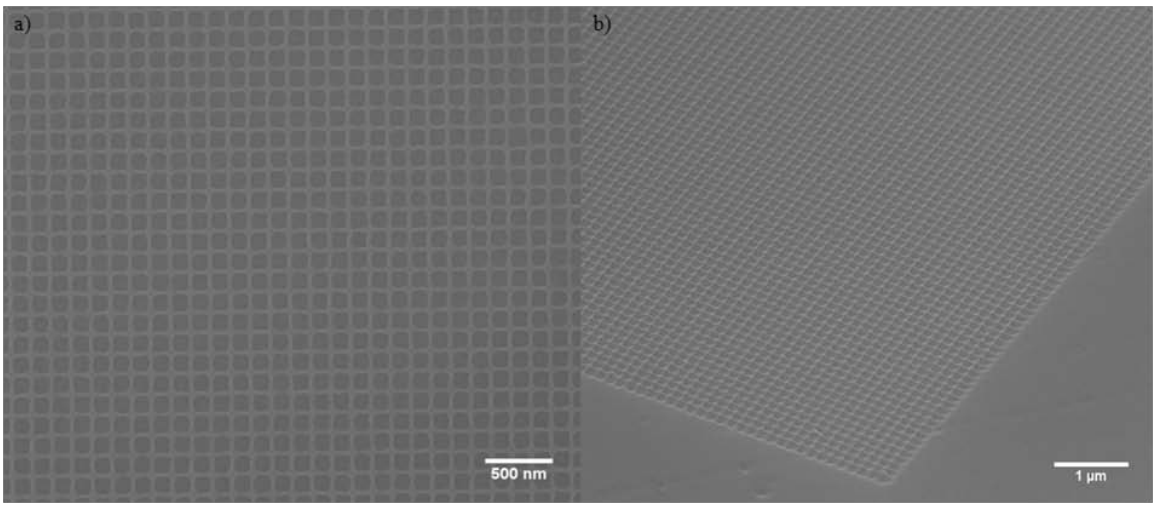

Figure 4-4: Transferred pattern on SiO_2 layer. (a) A Focus Ion Beam (FIB) image of transferred ~120nm square pattern on SiO_2 layer, after 5 min 100W CHF_3 etching and 10 min 50W oxygen etching to remove PMMA layer. (b) A 52 degree angle view of the transferred pattern with a depth of ~60 nm on SiO_2 layer.

4.4 Ion Beam Proximity Lithography

Ion beam proximity lithography is a low cost, high throughput, mass production way of producing high resolution patterns. In IBPL, a stencil mask with sparse pattern is exposed by a board beam of accelerated ions (He^+ in this project), the transmitted beamlets were tilted by controlled system to multiple print mask pattern [36], in order to generate a higher density pattern on substrate resist. A schematic of ion beam proximity lithography is shown in Figure 4-5.

To apply SLIM process in ion beam proximity lithography, non-circular patterns cannot be used as mask pattern because proximity effect will cause huge loss on corner resolution when pattern size is small enough. The solution is to use sparse dot pattern as mask, and run SLIM process after IBPL. The pre-defined precursor circle pattern in large area will be turned into non-circular ones at the same time in the following SLIM process.

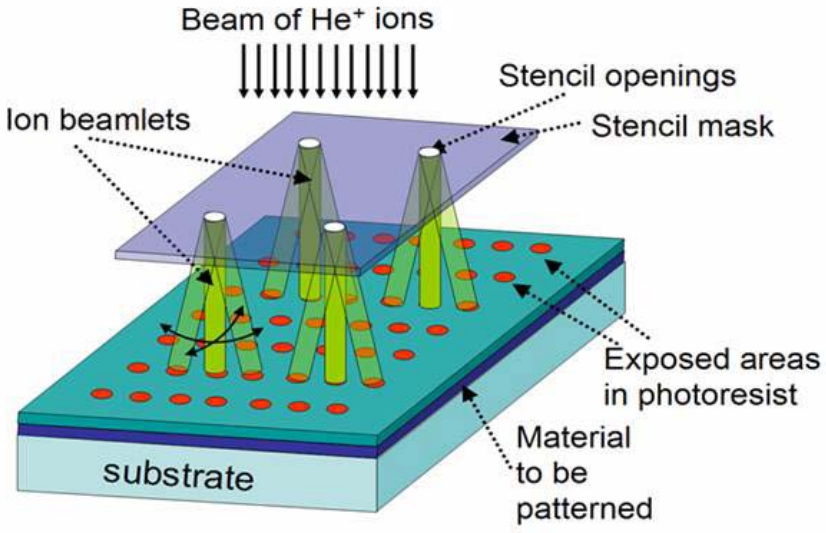

Figure 4-5: A sketch of ion beam proximity lithography printing multiple density patterns.

Mask fabrication is an essential step in IBPL. Parameters such as contrast, thickness, thermal stability and resolution should be compromised before the decision of mask material. The contrast of a stencil mask represents the deposited energy ratio of exposed and unexposed area. It will be influenced by the ion scattering near the pattern opening. Mask thickness determines its contrast as well as its thermal stability. A thicker mask will have better contrast since more scattered ions near opening are recaptured by the side wall, and better thermal stability. However, thick mask is usually difficult for fabrication and pattern transfer, and transfer a high resolution pattern from resist layer into a thick membrane usually will cause big resolution loss.

Silicon nitirde is a common used mask material in IBPL research [37], it was chosen because the easy preparation of fabrication (fabricate a SiN_x membrane is much easier than other material like Si, simple operation in pattern transfer by chemical reactive etching), stability (will not be oxidized, difficulty in react with gas in

environment) and high resolution. In my project, SiN_x wafer with 250nm SiN_x on both sides was chosen for the mask fabrication. Figure 4-6 illustrates the stencil mask fabrication process using silicon nitride membranes.

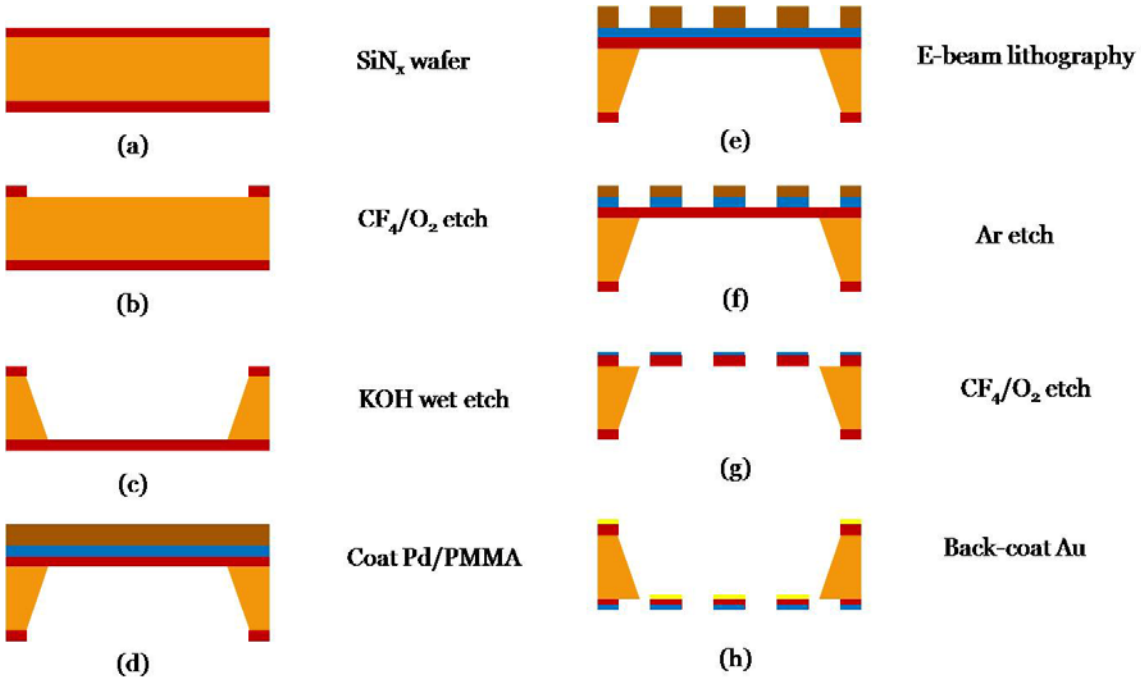

Figure 4-6: Process schematic, fabrication of SiN_x mask for ion beam proximity lithography.

The mask fabrication process starts with the fabrication of SiN_x membrane. First, a plastic mask with 1 inch by 1 inch square opening is printed, it is used to transfer the membrane opening into SiN_x layer. The SiN_x layer is then etched by a mixture gas of 0.8 mTorr CF_4 and 0.2 mTorr O_2, at 30 W for 30 minutes to remove the uncovered window opening SiN_x area. Si etch is carried out using 33% potassium hydroxide (KOH) maintained at 80°C for about 8 hour until all the Si under that window opening is removed. The produced membrane should be rinsed in 80°C deionized (DI) water for half an hour to prevent KOH re-crystallized on membrane. Another half an hour DI water

rinsing will clean residue and keep the membrane in a normal temperature, then we get a 250 nm thick SiN_x membrane.

After the fabrication of membrane, a 15nm thick palladium (Pd) layer is deposited on the membrane using a thermal evaporation system. The mask sample should be well mounted in evaporator chamber to keep both sides the same pressure, in order to keep the membrane safe in pumping and venting steps. The reason why Pd is chosen here instead of other material is because of its high selectivity in pattern transfer and stability from reaction with background gas. A 150nm PMMA layer is then spin-coated on followed by e-beam lithography to print the sparse dot array. The PMMA thickness here is characterized to ensure the protection of unexposed area of 100% over etch during pattern transferring. The defined resist is developed in a 3:1 solution of IPA : MIBK for 30 second, rinsed in IPA for another 30 second and dried in nitrogen.

Before we transfer mask pattern use RIE system, chamber cleaning working is run by oxygen clean and argon clean, consequently, at 5 mTorr and 30 W for 30 minutes each. This is to remove any possible contamination left in the chamber. In the following process, pattern is first transferred from PMMA layer into Pd layer, using argon etch at 1 mTorr and 13 W for about 10 minutes. Etch rate is measured by witness sample to ensure 100% over etch to make sure the complete pattern transfer into metal layer. Pattern is then transferred from Pd layer into SiN_x layer by mixture gas etching, 0.8 mTorr CF_4 and 0.2 mTorr O_2, at 30 W for about 40 minutes. The oxygen in the mixed gas will remove PMMA residue on Pd layer so the membrane now is made up of 250 nm SiN_x layer and a thin Pd layer on top of it. The last step of mask fabrication is to deposit a gold layer on the back side of the membrane using thermal evaporator.

The gold layer on the back side works as protection layer, which can strengthen the membrane and protect pattern side wall from ion bombardment. The gold layer also closes up the back side of pattern to make the opening size to a desired value. Figure 4-7 shows the a) topside and b) backside views of a SiN_x mask, with a pattern of 200 nm diameter dot and 1 um pitch. From the figure we can see that the topside view image has a larger size distribution (6.3%) than the backside view image (3.8%). This is because pattern size distribution is compromised a little when back cover gold layer closing up openings. The size distribution of printed pattern by IBPL can be further decreased by average printing technology and the future SLIM process.

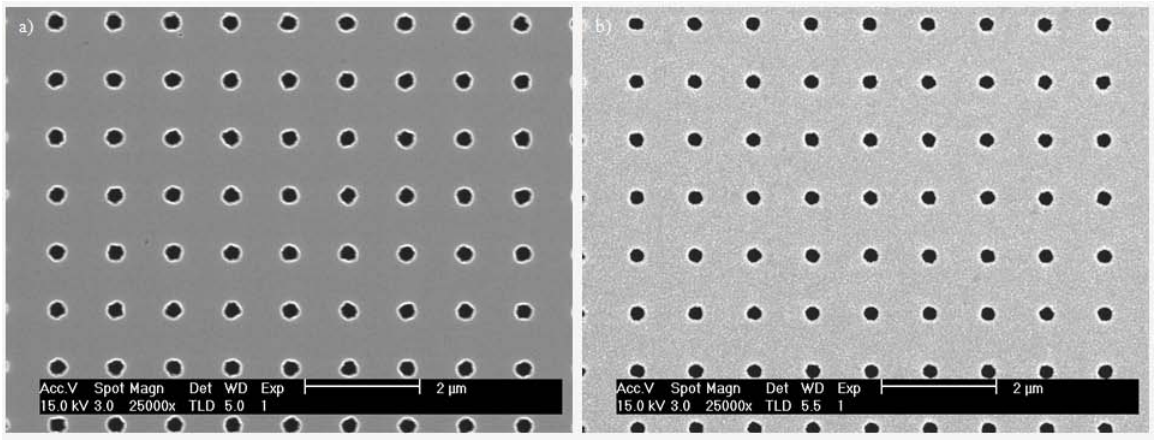

Figure 4-7: (a) Topside view of silicon nitride mask. (b) Backside view of silicon nitride mask, coated with a gold layer.

There are still several challenges for IBPL. Lithography resolution is limited by the distance between mask and sample resist, distance control is difficult because the membrane will be easily damaged by a single touch from the sample beneath. Nano-step system in IBPL should be well calibrated to control multiple printing. And the IBPL tool in our lab has a weak energy which can only print on PMMA layer less then 100nm thickness, this thickness means more difficulty in the future SLIM process.

4.5 Summary

The fast-paced development of the semiconductor and data storage industry require advanced nanofabrication technology. Despite its high resolution and accuracy, electron beam lithography is too slow for industry application. New lithography techniques such as directed self assembly, nanoimprint lithography and ion beam proximity lithography are promising ways for future master production level application. The high efficiency of the generating dot pattern in a large area makes it especially suitable for the combination with the SLIM process to produce non-circular patterns for BPM and other applications.

Chapter 5: Low Energy Ion Irradiation

5.1 Background

Including all the approaches introduced above, BPM fabrication techniques can be mainly divided into two categories, bottom-up method and top-down method. The bottom-up method uses lithography and reactive ion etching technology to pre-define patterns on a Si wafer. Then magnetic layers are deposited over the substrate, shown in figure 5-1. a. The magnetic material on top of pattern pillars is magnetically isolated from the material in pattern trench. This method produces well fabricated patterns on silicon demonstrating up to 3.3 Tb/in^2, but suffers from pattern randomly over growth which influences magnetic property of each pattern, to make switching field distribution (SFD) large, as shown in figure 5-1. b. And the trench material also has magnetic signal which contributes to a background noise, interferences signal from magnetic patterns.

Top-down method, on the other hand, deposits magnetic thin films on a flat, pristine substrate. In order to make a magnetic pattern isolated by non-magnetic material. A patterned mask is then used in the following etch. Although there is no randomly over growth and interference from trench material, this method has its own disadvantage. Magnetic material for recording media, such as Co, Fe, Pt, Pd and Cr, are extremely difficult for reactive etch. Sputtering etch used in top-down method causes the problem of large pattern shape distribution and material re-deposition. The wall on top edge of the pattern is shown in Figure 5-1. c,. These factors may influence magnetic property of each bit, resulting in a wide distribution of switching field of BPM.

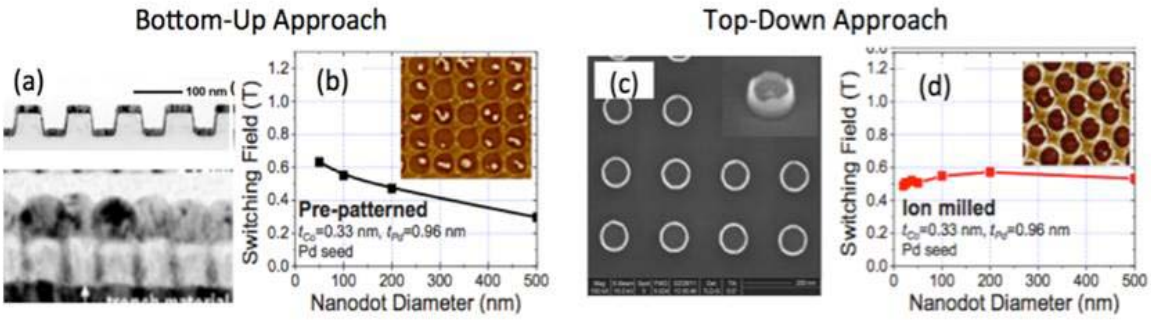

Figure 5-1: The bottom-up approach struggle with (a) trench material and overgrowth while the top-down approach struggle with (c) pattern transfer fidelity. Both must also deal with wide switching field distributions caused by (b) material growth and (d) ion damage [19, 38].

As discussed above, both fabrication methods have their advantages and disadvantages. To manufacture a qualified BPM with an areal density exceeding 1 Tb/in^2 and an acceptable SFD, a new fabrication technique for industry application is approached.

5.2 Low Energy Ion Irradiation

5.2.1 Introduction

Low energy ion irradiation is used as The new approach for BPM fabrication in my research project [39]. In the process, non-magnetic oxidation of magnetic material is deposited as the flat continuous thin film onto silicon wafer. A BPM mask is used in the following low energy ion etch. Low mass ions, such as hydrogen and helium, accelerated by a low energy, bombard the target surface and kick out the oxygen from the oxidation in the exposed area. Since the magnetic materials usually have heavy atoms compared to the oxygen, the transferred low energy will not influence them. In this case, the exposed parts become magnetic again while oxygen was removed from metal oxide after exposed iron irradiation.

Low energy ion irradiation is a manufacture compatible way to fabricate BPM. The defined magnetic pattern is isolate from each other by non-magnetic oxidation. So there is no interference signal from trench material. Magnetic bits are generated by removing oxygen from oxidation. No three dimensional fabrication such as pattern growing or etching is involved, resulting in low pattern size and shape distribution. The flat, continuous surface of bit patterned media, without any physically fabricated structure, is directly flyable for recording head. This means a lower distance between head and recording layer which is better for the head's read and write function. Compared to the recently popular ion implanting process, the low energy ions will not damage the film crystal structure.

5.2.2 Low energy helium irradiation

In my research project, helium is selected as the supply gas for the low energy ions because it is inactive with the target sample or background element. Helium is also considered for safety issue compared to hydrogen which may explode if mixed with oxygen. However, helium has disadvantages that we will discuss later in this section.

In low energy helium irradiation process, as shown in figure 5-2. a, cobalt oxide layer is sputtered onto a silicon substrate. Resist is spin-coated and pattern is defined by electron beam lithography. Helium ions are accelerated to a low energy level to strike the sample surface, bombarding uncovered area of the sample. The incoming particles are small enough to penetrate through the top surface layer and go deep into oxidation material. During this process, kinetic energy is transferred to different particles, particles will be knocked out. Energy transfer equation is described as following,

$$E_t = \frac{4m_1m_2}{(m_1+m_2)^2} E_a \ , \qquad (5\text{-}1)$$

where E_t is transfer energy, m_1 and m_2 are collided particles and E_a is energy of accelerated ions. When the transfer energy E_t of one particle is bigger than its displacement energy, the particle will be knocked out. In figure 5-2. a, when helium ions strike non-magnetic cobalt oxide layer, oxygen is removed from oxidization and material in the exposed area becomes cobalt with magnetic property again.

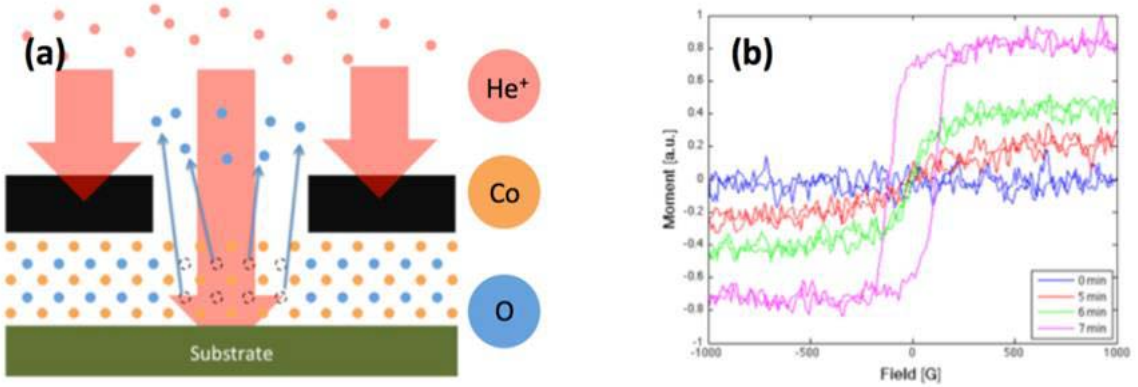

Figure 5-2: (a) Low-energy light ion irradiation is used to selectively liberate oxygen atoms from the lattice enabling (b) nonmagnetic Co_xO_y to be transformed into magnetic Co.

The experiment started without any patterned mask. The operation tool was RIE 180 and 300eV ions flux was generated by a working power of 100W. Target sample was a cobalt oxide layer with about 30 nm thickness sputtered on the top of a 10nm Ta layer as a seed layer on a silicon substrate. Cobalt was oxidized by oxygen during sputtering process and we did not investigate the detail of oxidized composition at this level because the film is too thin. The cobalt oxide layer was pre-measured in VSM to testify there was no magnetic signal, as shown in Figure 5-2. b. After several minutes under helium irradiation, as we can see in 5-2. b, magnetic loop was recovered. The signal reached its maximum value after 7 minutes' irradiation. This result demonstrates the effectiveness of the theory of low energy ion irradiation. With the protection of a mask on top, magnetic pattern can be selectively fabricated as desire.

5.2.3 SRIM simulation

Stopping and Range of Ions in Matter (SRIM) is a group of software which calculates interaction of ions with matters, with a core program called Transport of Ion in Matter (TRIM). SRIM is based on a Monte Carlo simulation method, namely the binary collision approximation with a randomly selection of parameters of colliding ions. It simulates collision and scattering of ions and target layers. SRIM was used to calculate parameters such as ion range in low energy ion irradiation, and to simulate interactions of low energy helium ions with cobalt oxide layer.

According to equation 5-1 above, transferred energy and displacement energy of different particles can be calculated as long as the ion energy is known. For 300eV helium ions irradiating cobalt oxide on top of tantalum seed layer, energy related to elements involved is listed in the table 5-1. Palladium is considered as well for the further purpose of application in Co/Pd multilayer. From the table we can see that energy transferred to oxygen is much higher than its displacement energy, so oxygen has a high sputtering yield in this process. The transferred Energy of cobalt and palladium is also higher than their displacement energy. Tantalum is the only element in simulation which has low transferred energy than its displacement energy.

Table 5-1: Critical energies for different elements in 300eV helium irradiation.

Element	O	Co	Pd	Ta
Transferred Energy (eV)	192	71.25	42	25.2
Displacement Energy (eV)	12.5	33.0	36.1	90.6

Since the detail composition of cobalt oxide is unknown, SRIM simulation is run for both CoO and Co_3O_4, two most popular cobalt oxides. The results are similar to each other, we can consider the average value of parameters as the corresponding to the cobalt oxide samples. Figure 5-3 is a 3D XY ion distribution image of 300eV helium ions striking Co_3O_4 layer. X is along the ion penetrate depth while Y is along axis parallel to the surface. Helium ions with 300eV energy go as deep as more than 10 nm inside cobalt oxide, but most of them are in the range of 38Å. Thickness of cobalt layer converted from cobalt oxide can be estimated by this simulation.

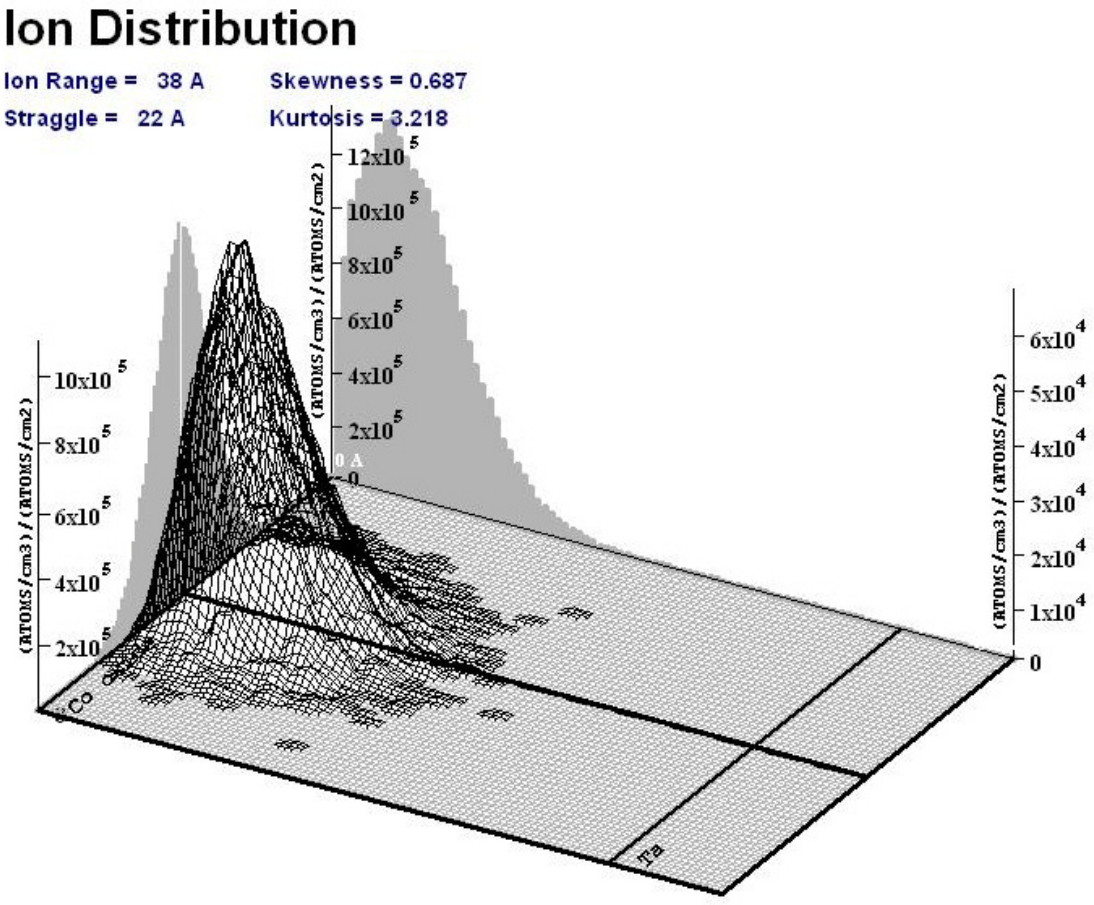

Figure 5-3: SRIM simulation of 300eV helium ions striking cobalt oxide layer.

From table 5-1 above, it is obvious that helium ions sputter away other materials while knocking oxygen out for magnetic recovery. The damage of other element besides

oxygen makes deposited thin film being etched away. An easy solution for this is to decrease the ion energy. We will discuss this later in this chapter.

5.3 Experiment and result

5.3.1 300eV helium irradiation

The processing tool of Low energy helium irradiation in my research project is an Oxford Plasma Lab ICP 180 RIE system. The working power is 100W to generate 300eV ion energy. For this system, Helium plasma is difficult and unstable to be ignited directly, so we introduced argon plasma to help the irradiation at the beginning of our process. The process contains two steps. System firstly ignites 100W argon plasma, for about 10 second, to wait until plasma becomes stable. Then it holds the plasma while changing supply gas with helium. In this case helium plasma is easily ignited and stable for irradiation process. However, since argon ions are big and heavy compared to those target materials in irradiation, the argon plasma step will physically remove material on the top surface and damage sample layer. This is bad for magnetic patterning especially when applied to the angstrom level multilayer. As a result, the lower energy and the shorter plasma time for argon, the damage is less as long as the helium plasma is stable. That is why second level argon plasma time was chosen.

Figure 5-4 shows magnetic loops of cobalt oxide with different helium irradiation time, measured by a Vibrating Sample Magnetometer (VSM). Data points are sampled from 5 minutes to 10 minutes. The non-magnetic cobalt oxide layer showed magnetic signal again after 5 minutes' helium irradiation. Signal increased with longer irradiation time, and reached its maximum value at 7 minutes. Then magnetic moment decreased in further irradiation and signal was lost at 10 minutes. The oxidation layer turned back into

cobalt while the helium ions stroke the cobalt oxide and kicked the oxygen out, So the sample layer become magnetic again. In the meanwhile, as we discussed above, 300eV helium ions still kept sputtering away part of cobalt, which means the layer was being etched away. When the layer thickness reached a certain value where there was no more cobalt oxide beneath, the effect of etching away cobalt became a main influence factor in the process. As layer thickness was decreasing, saturate magnetic moment also decreased.

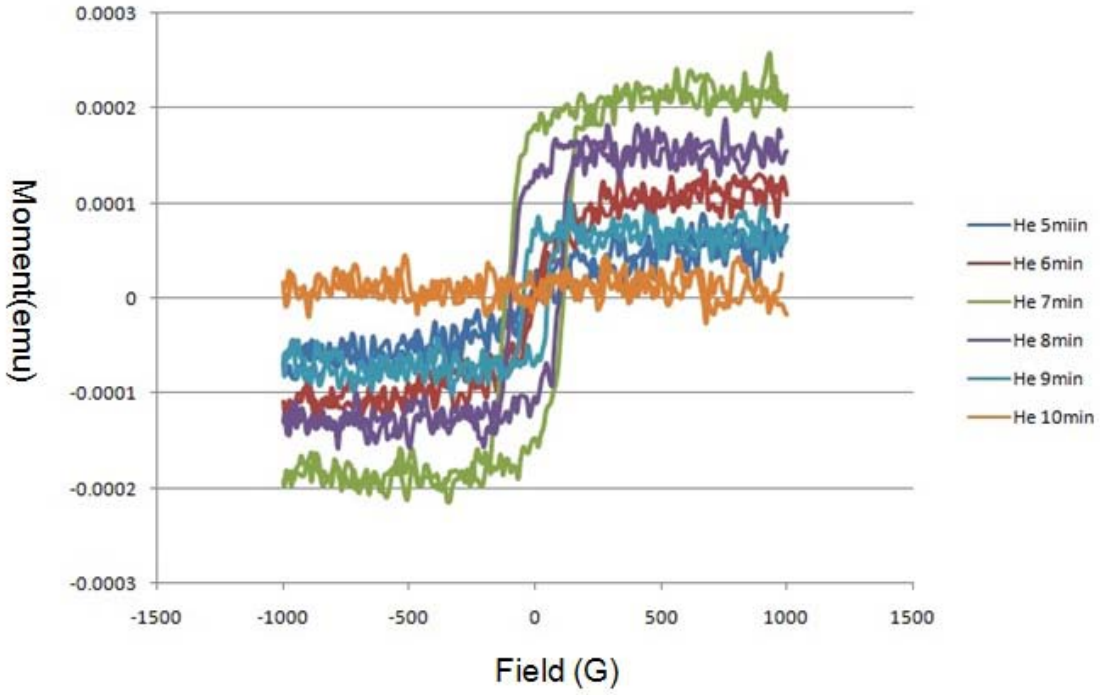

Figure 5-4: VSM measurements of recovered cobalt layer magnetic signals by 300eV helium irradiation.

The cobalt oxide layer is about 25nm, on top of a 5nm Ta seed layer. This Ta seed layer works as an adhesion layer and also provides a good surface roughness. Since I used the lowest oxygen gas rate, 3 sccm, to oxidize cobalt and make thin film non-magnetic, the composition of oxidation is unknown. In this case, we cannot calculate

magnetic moment in emu/g without accurate density. Sample size in the experiments is a half inch by half inch square piece. According to cobalt moment 1440 emu/cc and the data measured in VSM, we can estimate the recovered cobalt layer in irradiation process is about 8.6 Å which is less than SRIM simulation because SRIM does not count inner action.

5.3.2 120eV helium irradiation

Damage of cobalt from helium irradiation should be eliminated for the future application in multilayer magnetic patterning. According to the calculation and the working ability of RIE 180 system, a decrease of working power is decided. The new applied working power is 30W to generate ion energy of 120eV, resulting lower transferred energy, as shown in table 5-2. The decreased energy makes a lower transfer energy than the displacement energy for cobalt, but the two values are close which means there is still a small amount of cobalt will be removed.

Table 5-2: Critical energies for different elements in 120eV helium irradiation.

Element	O	Co	Pd	Ta
Transferred Energy (eV)	76.8	28.5	16.8	10.1
Displacement Energy (eV)	12.5	33.0	36.1	90.6

In figure 5-5, SRIM simulation on 120eV helium ions shows a smaller range, about 22 Å from the peak to the deepest one less than 10nm. Shorter ion range leads to a thinner film of recovered by cobalt but less damage to magnetic material like cobalt. Lower energy can be applied for further reduction of ion damage on cobalt layer, but it rises the

difficulty to ignit helium plasma in our RIE 180 system. Hydrogen can be used instead of helium in the further solution.Compared to the helium irradiation, Hydrogen irradiation will transfer much lower energy and proton can go deeper because of its smaller mass and size.

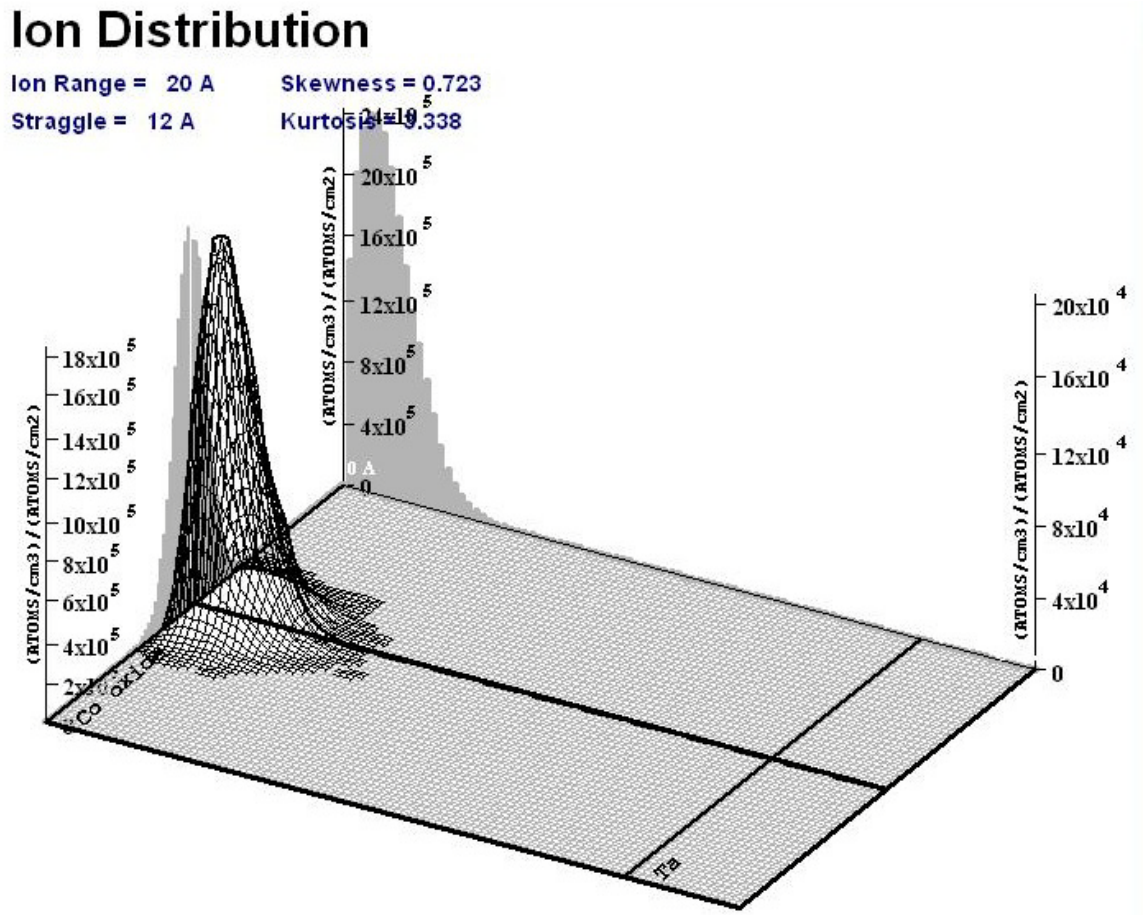

Figure 5-5: SRIM simulation of 120eV helium ions striking cobalt oxide layer.

Figure 5-6 shows magnetic signals of the same prepared sample using 120eV helium irradiation. Data sample ranges from 13 minutes to 20 minutes. Compared to the VSM result from 300eV irradiation experiment, the magnetic recovery became slower because the lower energy incoming ions lead to slower the removing rate and theshorter penetrate depth. This is also why magnetic signal survived longer. sample still carried magnetic moment after 20 minutes helium irradiation. We can notice that the maximum

saturate moment in Figure 5-6 is a little smaller than the one in Figure 5-4. This is acceptable because the lower ion energy results in smaller penetrate depth, and a thinner recovered cobalt layer. Using the same method above, we can calculate the estimated cobalt layer thickness is about 6.5 nm, it is less than the result from 300 eV irraidation because ions with lower energy penetrate shorter depth.

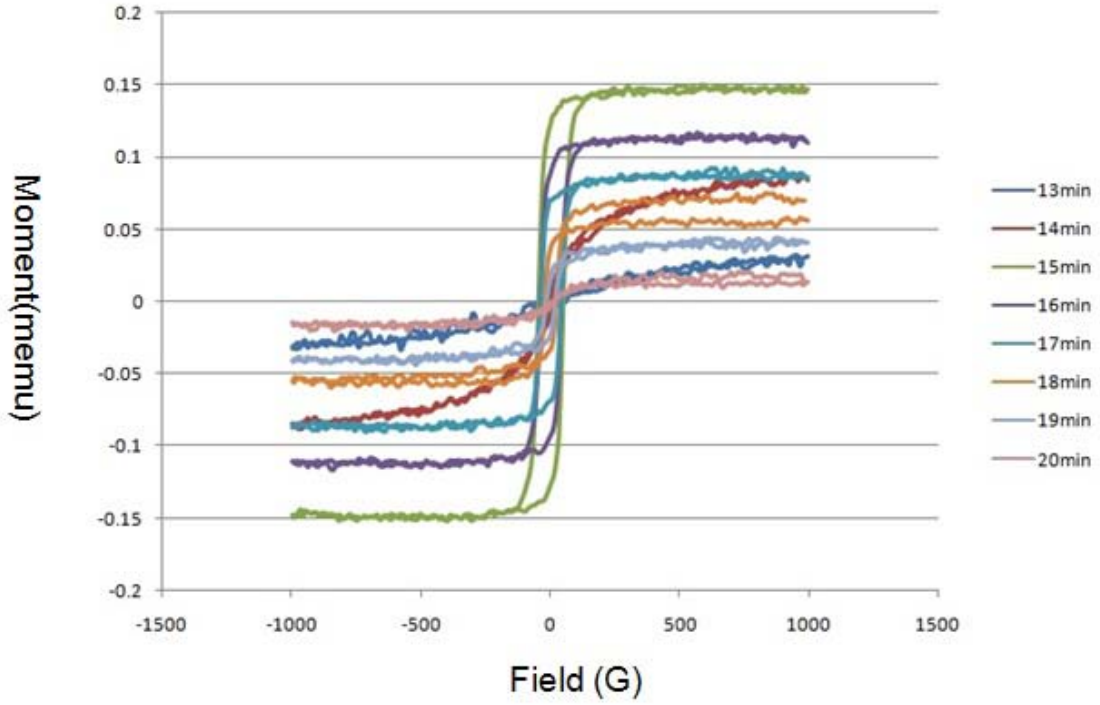

Figure 5-6: VSM measurements of recovered cobalt layer magnetic signals by 120eV helium irradiation.

Larger range experiment was done to investigate the relationship between saturate magnetic moment and etch time and the result is shown in Figure 5-7. According to the image, sample keeps non-magnetic for 6 minutes and becomes magnetic again after 8 minutes helium irradiation. Magnetic signal increases until it reaches its maximum value at 14 minutes, then decreases to non-magnetic again at 20 minutes. This experiment result proves the explanation above how helium, cobalt and oxygen interact in the

process. To produce a qualified bit patterned media, we should control the irradiation time at the point where the magnetic signal is biggest.

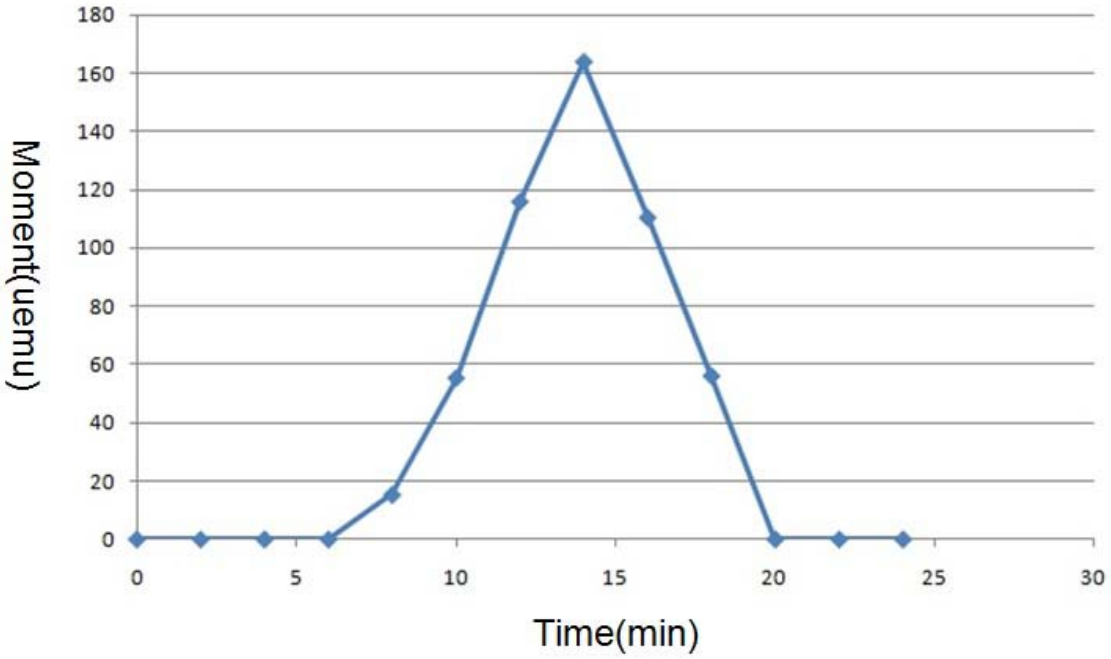

Figure 5-7: Magnetic moment vs etch time in 120eV helium irradiation.

5.3.3 Thin film surface analysis

Besides magnetic measurement, surface analysis tool were used to study low energy helium irradiation. The main goal for the surface analysis is to observe the change of oxidized layer before and after irradiation, and compare the recovered cobalt with not oxidized one. I also try to analyze composition of cobalt oxide since it is still unknown, but the film thickness is so thin that answer is not clear enough.

Figure 5-8 shows X-ray photoelectron spectroscopy (XPS) measurement results of cobalt, cobalt oxide before and after helium irradiation. Samples were heated to 300°C to remove water vapor and other OH based compound. There is no sputtering system inside

the XPS so oxidization of sample surface layer is inevitable, background influence also contributes to part of oxygen signal we got.

Measurements were run for oxygen peak and cobalt peak respectively. For oxygen peak, according to XPS reference book, bonding energy between 528 and 531eV represents metal oxide, and signal larger than 532eV comes from background influence. As we can see in the left side oxygen peak graph, it is obviously that cobalt oxide has the highest metal oxide peak. Cobalt at 300°C also has a peak maybe because the high temperature accelerated oxidation by background oxygen. Original cobalt has a small peak possibly because sample was oxidized before measurement by air. There is almost no peak for cobalt oxide after helium irradiation, which supports the assumption that oxygen has been removed from the original material.

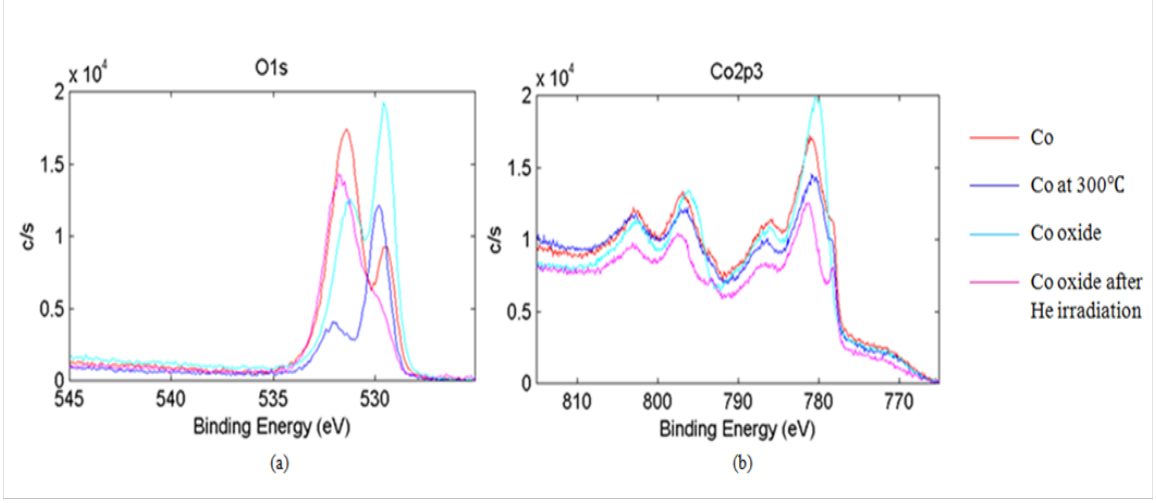

Figure 5-8: XPS analysis of cobalt, cobalt oxide before and after helium irradiation.

For cobalt peak measurement, 778eV is cobalt peak and binding energy from 780 to 782eV stands for cobalt oxide and cobalt hydroxide compound. The curve for cobalt oxide after helium irradiation is the lowest one because it has least cobalt element after helium ions etching away part of the cobalt from material. However, despite the lowest

signal, cobalt after helium irradiation has the most obvious peak at 778eV. On the other hand, cobalt oxide has the highest peak for cobalt oxide and cobalt hydroxide compound. Cobalt measurement again proves the theory of low energy ion irradiation works.

X-ray Diffraction (XRD) is used to analyze crystal structure of the same prepared sample as above. The goal for the measurement is to prove the irradiation theory, as well as the composition of material before and after helium irradiation. The result is shown in Figure 5-9. Strong Co (220) FCC peak is observed in cobalt after irradiation curve, and peak CoO (111) is only found in CoO curve. The curve of cobalt and cobalt oxide after irradiation is mostly the similar. There are other small peaks in the graph which support the low energy ion irradiation theory, but there are also some peaks we cannot identified. From this XRD result, it is difficult to tell what exactly inside the cobalt oxide, because of the lack of peak identification. This may be because X-ray goes too deep into sample, probably several microns. However, the thickness of my sample is just about 30 nm, and the estimated recover cobalt layer is only several nanometers thick. In this case, the signal is too weak to be measured and analyzed.

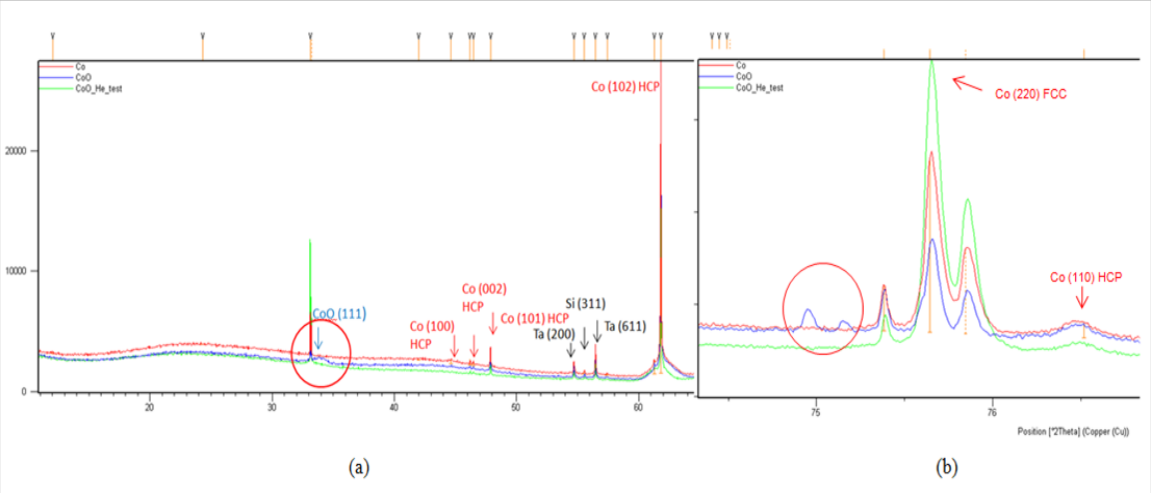

Figure 5-9: XRD analysis of cobalt, cobalt oxide before and after helium irradiation.

5.3.4 Tantalum cap layer

Besides serving as a seed layer, tantalum is also a good selection of cap layer to protect magnetic layer underneath from oxidation. Otherwise for material like cobalt, re-oxidation of recovered cobalt will damage magnetic patterning process. And for my project, since the future goal is to combine low energy ion irradiation with SLIM to fabricate non-circular magnetic pattern for the bit patterned media, an extra argon etch is expected. In this case, to avoid magnetic layer damage by argon plasma while turning dot array into square pattern, tantalum layer also works as a sacrificial layer. It should be able to survive SLIM argon etch and remain a thin layer on top to protect cobalt layer from oxidation. This cap layer cannot be too thick, because a thick top layer decreases helium ion penetration depth in cobalt oxide layer, resulting a thinner recovered layer and lower magnetic signal.

The etch rate of tantalum in RIE 100 plus, system for SLIM process, is several angstroms per minute. The value is not so accurate because it changes with environment condition. As a result, since most argon etches in SLIM process take about 4 minutes, 15 angstrom was chosen as the tantalum cap layer thickness. SRIM simulation for 120eV helium ions striking sample with a cap layer is shown in Figure 5-10. We can see that the ion range only changes a little, which means tantalum cap layer does not prevent ion penetration while working as a protection layer.

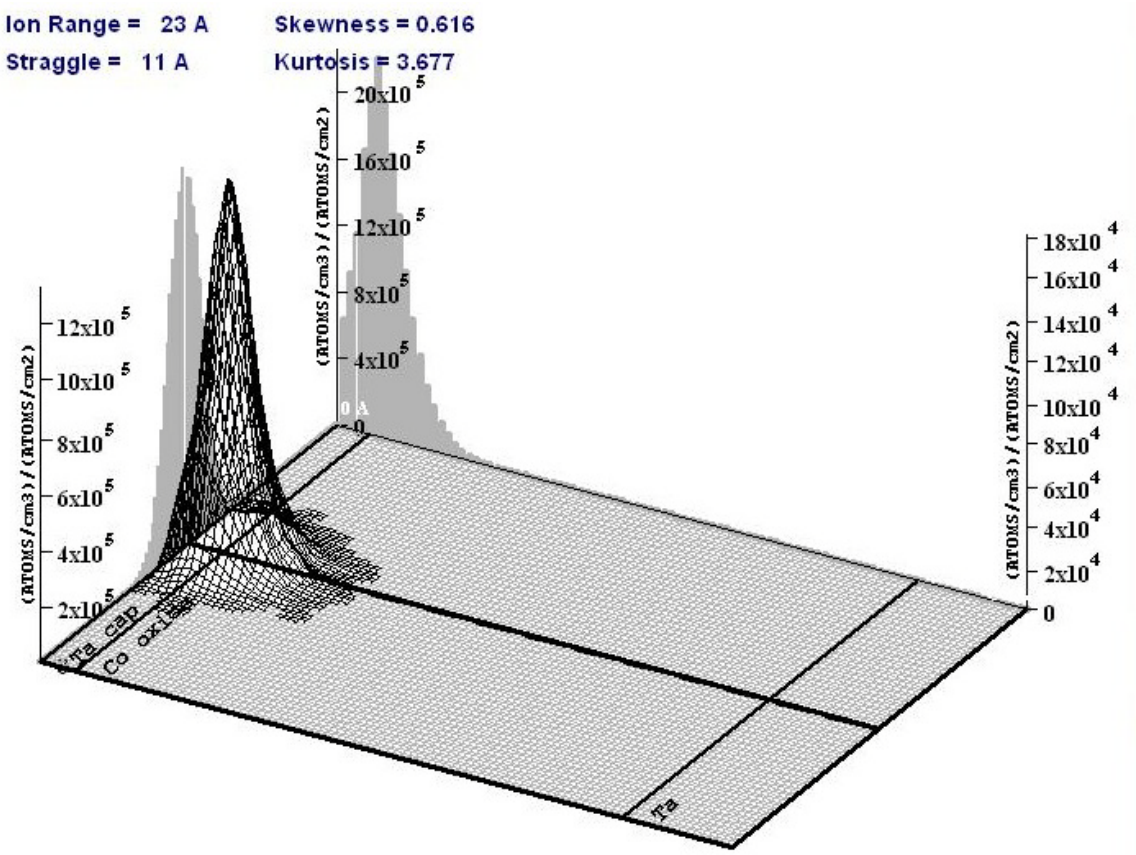

Figure 5-10: SRIM simulation of 120eV helium ions striking cobalt oxide layer with a 15 angstrom tantalum cap layer.

Figure 5-11 show results of magnetic moment change with irradiation time with and without tantalum cap layer. Both samples were etched in argon plasma for 4 minutes before helium irradiation. From the graph we can see that with the protection of cap layer, magnetic signal increased a lot, almost tripled the value without cap layer. This is because helium ions sputter away recovered cobalt while removing oxygen from cobalt oxides, and Ta cap layer protects cobalt layer, leading to a relatively thicker recovered cobalt layer. This also explains why sample with Ta cap layer firstly appeared magnetic signal. As the irradiation went on, both magnetic signals decreased. However, signal from the sample with cap layer rose again after reaching its minimum value at 18 minutes. The possible explanation for this is after 18 minutes helium irradiation, the tantalum cap layer

is consumed out. At this time, the sample became a cobalt oxide layer with a thin layer of recovered cobalt on top. Magnetic signal went up again later by helium irradiation and would go down at some certain point. This experiment proves that using a tantalum cap layer is necessary and better for magnetic patterning.

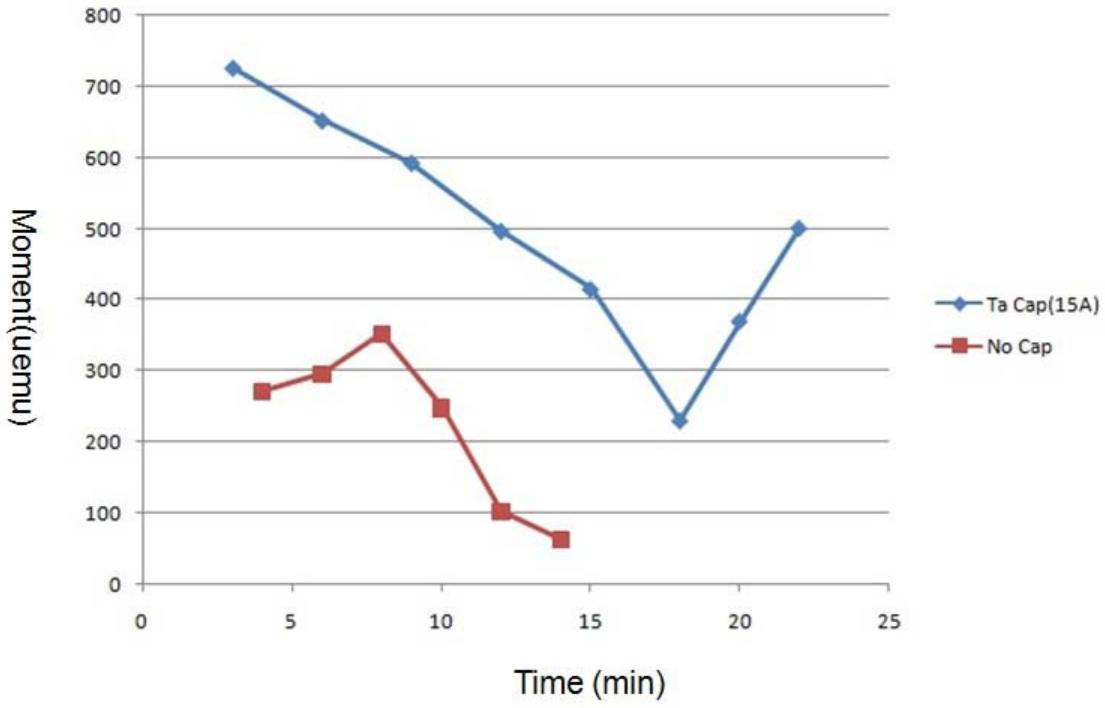

Figure 5-11: Comparison of magnetic moment vs etch time in 120eV helium irradiation with and without tantalum cap layer.

5.3.5 Magnetic patterning

All the above experiments and results came from continuous thin film. However, besides the magnetic property investigation, pattern fabrication is another essential step in producing non-circular BPM using low energy ion irradiation. Extra argon etching in low energy ion irradiation was pre-demonstrated for the purpose of using SLIM. Graphited PMMA surface layer by argon plasma can protect resist from high etch rate of helium

plasma. Figure 5-12 shows fabrication results of square pattern through argon SLIM process and low energy helium irradiation.

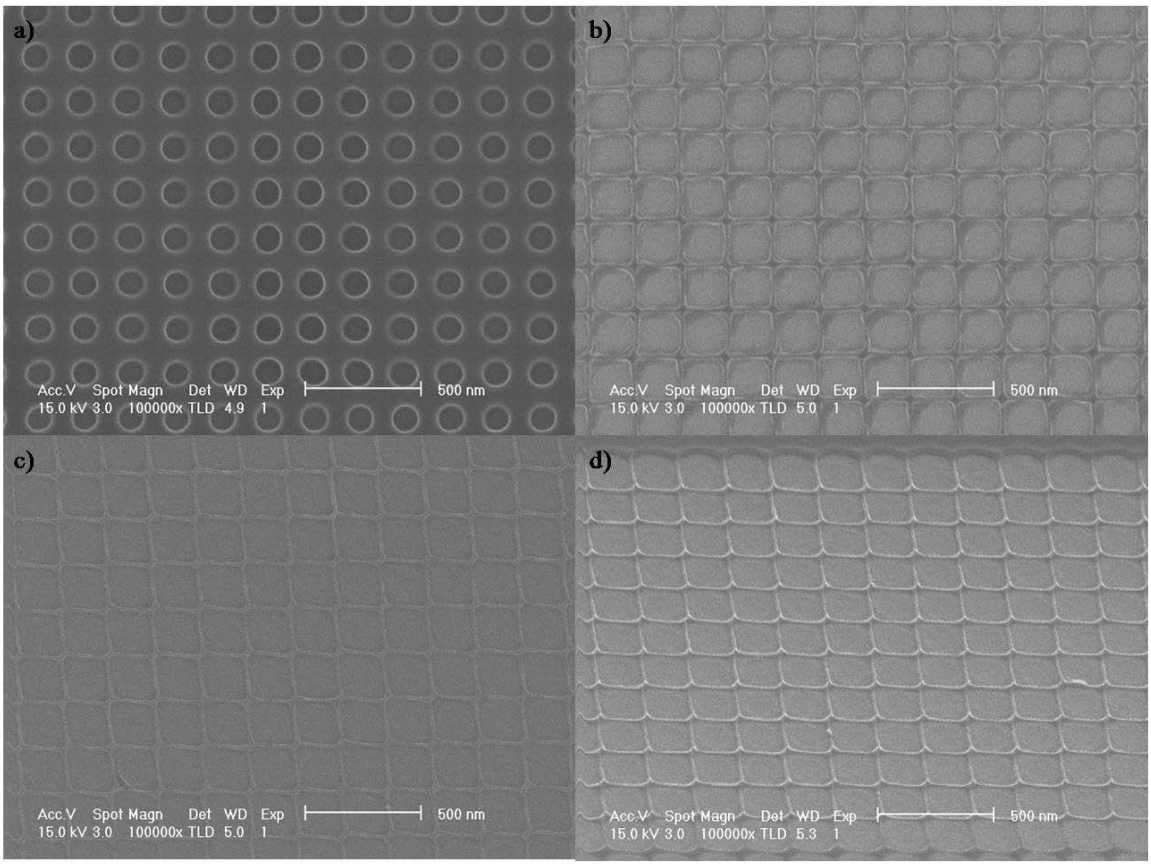

Figure 5-12: Pattern fabrication using SLIM and low energy helium irradiation. (a) Original dot array with 137nm diameter and 200nm pitch. (b) Square pattern after 4 minutes' argon etching. (c) Square pattern after 3 minutes' helium irradiation. (d) Angle view of square pattern after helium irradiation.

5.4 Summary and Future work

Low energy ion irradiation was proved to be a promising candidate of future BPM fabrication technique. However, despite the low sputtering yield, cobalt is still being removed from thin film material by helium ions. This is going to be a major issue when experiment involves multilayer in angstrom level. A good solution is to use hydrogen instead although hydrogen has several disadvantages. For example, when a leakage

happens, mixture of hydrogen and oxygen in air is extremely dangerous. Its explosion property calls for serious safety concern. Hydrogen also reacts with materials like silicon, forming byproduct to contaminate sample. Low energy proton irradiation is theoretical better because proton is smaller than helium ion and with less mass. With the same energy, proton can travel deeper in target material, knocking out oxygen without much damage of other elements.

Another future research work is multilayer patterning with ion irradiation. Magnetic recording media is made by optimized magnetic multilayer to produce large coercivity. Multilayer such as FePt and CoPd are popular because they have such a high coercivity which none of single material has. This is very important since larger coercivity means better thermal stability. FePt is not suitable for ion irradiation because Fe oxide is magnetic. So the future research work should investigate the application on CoPd multilayer.

Chapter 6: Conclusion

A new way of fabricating non-circular nanostructure is demonstrated. This SLIM process uses pattern on PMMA layer as a precursor which is pre-defined by e-beam lithography. The following argon plasma etching (RIE)depletes oxygen and hydrogen in resist to graphitize the surface layer of PMMA. The self-limited phenomenon observed in lateral etching makes the well defined self-assembled non-circular pattern scalable. This technique overcomes the proximity effect in e-beam lithography and provides a low cost way of producing sub-100nm close-packed non-circular pattern with high spatial resolution. SLIM application in BPM fabrication increases recording density and pattern area, resulting in stronger thermal ability. The technique has great potential in any fabrication industry requiring non-circular patterns.

Investigation on SLIM process was carried on. Results of experiments with different parameters were fitted and analyzed to optimize process control. The 75nm square pattern was successfully fabricated according to the optimal recipe. PMMA surface layer composition change was demonstrated to be a function of etching rate and heat resistivity. The well shaped nanostructure from nickel and permalloy evaporation was demonstrated. The CoPd multilayer pattern was deposited by sputtering deposition. The SLIM process combination with ion beam proximity lithography and nanoimprint template manufacture is testified.

Investigation on low energy ion irradiation is undergoing. Helium irradiation process was studied on continuous cobalt oxide film with different accelerate energy. Magnetic property was recovered from non-magnetic oxide layer by irradiation removing oxygen from the material. Magnetic patterning combining SLIM and low energy ion

irradiation is under investigation. The future work will use hydrogen during the etching process instead of helium because of its lower mass and smaller size which will result in low energy proton irradiation on CoPd multilayer for BPM fabrication.

Reference

[1] H. N. Bertram and M. Williams, "SNR and density limit estimates: a comparison of longitudinal and perpendicular recording," *Magnetics, IEEE Transactions on*, vol. 36, pp. 4-9, 2000.

[2] S. N. Piramanayagam and Tom C. Chang, "Developments in Data Storage: Materials Perspective," *Platinum Metals Review*, vol. 56, pp. 262-266, 2012.

[3] D. Litvinov, R. M. Chomko, L. Abelmann, K. Ramstock, G. Chen, and S. Khizroev, "Micromagnetics of a soft underlayer," *Magnetics, IEEE Transactions on*, vol. 36, pp. 2483-2485, 2000.

[4] "Introduction to perpendicular recording." *Guzik-Magnetic Recording Systems and Measurements*, Internet: http://www.guzik.com/solutions_chapter7.asp, Jan. 27, 2005

[5] C. P. Bean and J. D. Livingston, "Superparamagnetism," *Journal of Applied Physics*, vol. 30, pp. S120-S129, 1959.

[6] C. Ross, "PATTERNED MAGNETIC RECORDING MEDIA," *Annual Review of Materials Research*, vol. 31, pp. 203-235, 2001.

[7] R. E. Rottmayer, S. Batra, D. Buechel, W. A. Challener, J. Hohlfeld, Y. Kubota, Lei Li, Lu Bin, C. Mihalcea, Keith Mountfield, Kalman Pelhos, Chubing Peng, T. Rausch, Michael A. Seigler, D. Weller and XiaoMin Yang. "Heat-Assisted Magnetic Recording," *Magnetics, IEEE Transactions on*, vol. 42, pp. 2417-2421, 2006.

[8] Robin Harris. "Engineering the 10 TB notebook drive" Internet: http://www.zdnet.com/blog/storage/engineering-the-10-tb-notebook-drive/194, Sep. 27,2007.

[9] G. F. Hughes, "Patterned media write designs," *Magnetics, IEEE Transactions on*, vol. 36, pp. 521-527, 2000.

[10] B. D. Terris, T. Thomson, and G. Hu, "Patterned media for future magnetic data storage," *Microsystem Technologies*, vol. 13, pp. 189-196, 2007/01/01 2007.

[11] R. Wood, M. Williams, A. Kavcic, and J. Miles, "The Feasibility of Magnetic Recording at 10 Terabits Per Square Inch on Conventional Media," *Magnetics, IEEE Transactions on*, vol. 45, pp. 917-923, 2009.

[12] P. Bruno, "Theory of interlayer magnetic coupling," *Physical Review B*, vol. 52, pp. 411-439, 07/01/ 1995.

[13] T. H. P. Chang, "Proximity effect in electron beam lithography," *Journal of Vacuum Science and Technology*, vol. 12, pp. 1271-1275, 1975.

[14] G. Owen and P. Rissman, "Proximity effect correction for electron beam lithography by equalization of background dose," *Journal of Applied Physics*, vol. 54, pp. 3573-3581, 1983.

[15] G. Owen, "Methods for proximity effect correction in electron lithography," *Journal of Vacuum Science & Technology B: Microelectronics and Nanometer Structures*, vol. 8, pp. 1889-1892, 1990.

[16] V. A. Parekh, A. Ruiz, P. Ruchhoeft, S. Brankovic, and D. Litvinov, "Close-Packed Noncircular Nanodevice Pattern Generation by Self-Limiting Ion-Mill Process," *Nano Letters*, vol. 7, pp. 3246-3248, 2007/10/01 2007.

[17] R. L. Bruce, S. Engelmann, T. Lin, T. Kwon, R. J. Phaneuf, G. S. Oehrlein, B. K. Long, C. G. Willson, J. J. Vegh, D. Nest, D. B. Graves and A. Alizadeh. "Study of ion and vacuum ultraviolet-induced effects on styrene- and ester-based polymers exposed to argon plasma," *Journal of Vacuum Science & Technology B: Microelectronics and Nanometer Structures*, vol. 27, pp. 1142-1155, 2009.

[18] S. Shivkumar, X. Yao, and M. Makhlouf, "Polymer-melt interactions during casting formation in the lost foam process," *Journal Name: Scripta Metallurgica et Materialia; Journal Volume: 33; Journal Issue: 1; Other Information: PBD: 1 Jul 1995*, pp. Medium: X; Size: pp. 39-46, 1995.

[19] O. Hellwig, J. K. Bosworth, E. Dobisz, D. Kercher, T. Hauet, G. Zeltzer, J. D. Risner-Jamtgaard, D. Yaney and R. Ruiz. "Bit patterned media based on block copolymer directed assembly with narrow magnetic switching field distribution," *Applied Physics Letters*, vol. 96, pp. 052511-052511-3, 2010.

[20] H. A. Klok and S. Lecommandoux, "Supramolecular Materials via Block Copolymer Self-Assembly," *Advanced Materials*, vol. 13, pp. 1217-1229, 2001.

[21] C. Vieu, F. Carcenac, A. Pépin, Y. Chen, M. Mejias, A. Lebib, L. Manin-Ferlazzo, L. Couraud and H. Launois. "Electron beam lithography: resolution limits and applications," *Applied Surface Science*, vol. 164, pp. 111-117, 9/1/ 2000.

[22] F. A. Lowenheim and J. Davis, "Modern Electroplating," *Journal of The Electrochemical Society*, vol. 121, p. 397C, January 1, 1974 1974.

[23] S.-W. Chung, J.-W. Shin, Y.-K. Kim, and B.-S. Han, "Design and fabrication of micromirror supported by electroplated nickel posts," *Sensors and Actuators A: Physical,* vol. 54, pp. 464-467, 6// 1996.

[24] A. C. Chialvo, W. E. Triaca, and A. J. Arvia, "Changes in the electrochemical response of noble metals produced by square-wave potential perturbations: A new technique for the preparation of reproducible electrode surfaces of interest in electrocatalysis," *Journal of Electroanalytical Chemistry and Interfacial Electrochemistry,* vol. 146, pp. 93-108, 4/8/ 1983.

[25] Z. Wu, Z. Chen, X. Du, J. M. Logan, J. Sippel, M. Nikolou, Katalin Kamaras, John R. Reynolds, David B. Tanner, Arthur F. Hebard and Andrew G. Rinzler. "Transparent, Conductive Carbon Nanotube Films," *Science,* vol. 305, pp. 1273-1276, August 27, 2004 2004.

[26] H. Nishihara, T. Kwon, Y. Fukura, W. Nakayama, Y. Hoshikawa, S. Iwamura, N. Nishiyama, T. Itoh and T. Kyotani. "Fabrication of a Highly Conductive Ordered Porous Electrode by Carbon-Coating of a Continuous Mesoporous Silica Film," *Chemistry of Materials,* vol. 23, pp. 3144-3151, 2011/07/12 2011.

[27] N. Lupu, H. Chiriac, and P. Pascariu, "Electrochemical deposition of FeGa/NiFe magnetic multilayered films and nanowire arrays," *Journal of Applied Physics,* vol. 103, pp. 07B511-3, 04/01/ 2008.

[28] A. Ciszewski, S. Posluszny, G. Milczarek, and M. Baraniak, "Effects of saccharin and quaternary ammonium chlorides on the electrodeposition of nickel from a Watts-type electrolyte," *Surface and Coatings Technology,* vol. 183, pp. 127-133, 5/24/ 2004.

[29] F. J. A. Den Broeder, H. C. Donkersloot, H. J. G. Draaisma, and W. J. M. de Jonge, "Magnetic properties and structure of Pd/Co and Pd/Fe multilayers," *Journal of Applied Physics,* vol. 61, pp. 4317-4319, 1987.

[30] M. Li and C. K. Ober, "Block copolymer patterns and templates," *Materials Today,* vol. 9, pp. 30-39, 9// 2006.

[31] R. Ruiz, H. Kang, F. A. Detcheverry, E. Dobisz, D. S. Kercher, T. R. Albrecht, Juan J. de Pablo and Paul F. Nealey. "Density Multiplication and Improved Lithography by Directed Block Copolymer Assembly," *Science,* vol. 321, pp. 936-939, August 15, 2008 2008.

[32] X. Yang, L. Wan, S. Xiao, Y. Xu, and D. K. Weller, "Directed Block Copolymer Assembly versus Electron Beam Lithography for Bit-Patterned Media with Areal Density of 1 Terabit/inch2 and Beyond," *ACS Nano,* vol. 3, pp. 1844-1858, 2009/07/28 2009.

[33] K. Naito, H. Hieda, M. Sakurai, Y. Kamata, and K. Asakawa, "2.5-inch disk patterned media prepared by an artificially assisted self-assembling method," *Magnetics, IEEE Transactions on,* vol. 38, pp. 1949-1951, 2002.

[34] J. Moritz, S. Landis, J. C. Toussaint, P. Bayle-Guillemaud, B. Rodmacq, G. Casali, A. Lebib, Y. Chen, J. P. Nozires and B. Dieny. "Patterned media made from pre-etched wafers: a promising route toward ultrahigh-density magnetic recording," *Magnetics, IEEE Transactions on,* vol. 38, pp. 1731-1736, 2002.

[35] N. R. Rueger, J. J. Beulens, M. Schaepkens, M. F. Doemling, J. M. Mirza, T. E. F. M. Standaert and G. S. Oehrlein. "Role of steady state fluorocarbon films in the etching of silicon dioxide using CHF_3 in an inductively coupled plasma reactor,"

Journal of Vacuum Science & Technology A: Vacuum, Surfaces, and Films, vol. 15, pp. 1881-1889, 1997.

[36] J. C. Wolfe, S. V. Pendharkar, P. Ruchhoeft, S. Sen, M. D. Morgan, W. E. Horne, R. C. Tiberio and John N. Randall. "A proximity ion beam lithography process for high density nanostructures," *Journal of Vacuum Science & Technology B: Microelectronics and Nanometer Structures*, vol. 14, pp. 3896-3899, 1996.

[37] J. N. Randall, D. C. Flanders, N. P. Economou, J. P. Donnelly, and E. I. Bromley, "Silicon nitride stencil masks for high resolution ion lithography proximity printing," *Journal of Vacuum Science & Technology B: Microelectronics and Nanometer Structures*, vol. 1, pp. 1152-1155, 1983.

[38] Y. Shiroishi, K. Fukuda, I. Tagawa, H. Iwasaki, S. Takenoiri, H. Tanaka, H. Mutoh and N. Yoshikawa. "Future Options for HDD Storage," *Magnetics, IEEE Transactions on*, vol. 45, pp. 3816-3822, 2009.

[39] S. Kim, S. Lee, J. Ko, J. Son, M. Kim, S. Kang and J. Hong. "Nanoscale patterning of complex magnetic nanostructures by reduction with low-energy protons," *Nat Nanotechnol*, vol. 7, pp. 567-71, Sep 2012.